SINGLE CELL COMPENDIUM OF MUSCLE MICROENVIRONMENT IN PERIPHERAL ARTERY DISEASE REVEALS ALTERED ENDOTHELIAL DIVERSITY AND LYVE1^{+} MACROPHAGE ACTIVATION

Short title: scRNAseq of human skeletal muscle in PAD

Guillermo Turiel[1], Thibaut Desgeorges[1], Evi Masschelein[1], Zheng Fan[1,2], David Lussi[1], Christophe M. Capelle[3], Giulia Bernardini[4], Raphaela Ardicoglu[1], Katharina Schönberger[1], Manuela Birrer[5], Sandro F. Fucentese[6], Jing Zhang[1], Daniela Latorre[3,7], Stephan Engelberger[5], Katrien De Bock[1]

Affiliations: (1) Laboratory of Exercise and Health, Department of Health Sciences and Technology, Swiss Federal Institute of Technology (ETH), Zurich (Schwerzenbach), Switzerland; (2) Institute of Anatomy, University of Zurich, Zurich, Switzerland; (3) Institute of Microbiology, Department of Biology, Swiss Federal Institute of Technology (ETH), Zurich, Switzerland; (4) Zentrum für Gefässchirurgie, Kantonsspital Aarau, Aarau, Switzerland; (5) Vascular Center, Department for General, Visceral and Vascular Surgery, Kantonsspital Baden, Baden, Switzerland; (6) Department of Orthopedics, University Hospital Balgrist, University of Zurich, Zurich, Switzerland. (7) Institute of Experimental Neurology, Division of Neuroscience, IRCCS Ospedale San Raffaele (OSR), Milan, Italy.

Corresponding author:

Katrien De Bock

Email: katrien-debock@ethz.ch

Laboratory of Exercise and Health

Institute of Movement Sciences (D-HEST)

ETH Zürich - Swiss Federal Institute of Technology

ETH Zürich, SLA C7

Schorenstrasse 16

CH-8603 Schwerzenbach

Switzerland

Tel. +41 44 655 7389

ABSTRACT

Peripheral artery disease (PAD) results from atherosclerosis and chronic narrowing of lower limb arteries leading to decreased muscle perfusion. Current treatments are suboptimal, partly due to limited understanding of PAD muscle pathology. Here we use scRNAseq and spatial transcriptomics to analyze the composition of the muscle microenvironment in non-ischemic and PAD patients. We identified *ATF3/4*$^{+}$ endothelial cells (ECs) that exhibit altered angiogenic and immune regulatory profiles during PAD and confirmed that ATF4 signaling in ECs is required for effective ischemia recovery. Also, capillary ECs display features of endothelial-to-mesenchymal transition. Furthermore, *LYVE1*^{hi}MHCII^{low} macrophages are the dominant macrophage population in human muscle, adopting a more pro-inflammatory profile during PAD. Finally, we analyzed alterations in intercellular communication within the muscle microenvironment during PAD and confirmed that EC-derived factors can influence macrophage polarization. This dataset deeply characterizes the PAD muscle microenvironment and provides a resource for exploration of targeted therapies.

Introduction

Peripheral artery disease (PAD) is caused by atherosclerosis and chronic narrowing of lower limb arteries leading to decreased muscle perfusion and oxygenation. Cardiovascular risk factors, such as hypertension, hyperlipidemia and diabetes mellitus are important driving risk factors of PAD and patients often present other cardiovascular diseases[1]. PAD patients suffer from pain and fatigue in the limb muscles due to exercise-induced ischemia which resolves after a short period of rest, a syndrome termed intermittent claudication (IC)[2,3]. If left untreated or in more severe stages, persistent lack of limb perfusion can lead to critical limb ischemia (CLI), which comprises rest pain, tissue loss and necrosis, and ulcerations, which often progresses to amputation[1]. Current guidelines for treating PAD target large atherosclerotic lesions in the feeding arteries, but long-term clinical outcomes have been suboptimal, and many patients suffer from adverse events[4].

One potential reason for this might be that there is underlying skeletal muscle and vascular pathology in PAD[3]. Indeed, microvascular dysfunction has been reported, with abnormal microvascular architecture and fibrosis and few studies recently reported partial endothelial-to-mesenchymal (EndoMT) transition in PAD patients[5,6] and capillaries of end-stage patients[6]. Also, impaired vasoreactive responses might impair oxygen and nutrient delivery into the ischemic muscle[7]. Interestingly, some[8–11] but not all[12,13] studies observed increased vascular density. While the discrepancy underlying these conflicting observations is unclear, persistent ischemia in PAD patients despite increased vascularization nonetheless suggests that an active angiogenic response does not resolve tissue ischemia.

Studies using preclinical muscle injury models showed that microvascular endothelial cells (ECs) are not only essential for inducing muscle revascularization, ECs also steer muscle regeneration by interacting with other cells in their microenvironment. ECs activate muscle stem cells[14], control vascular tone through interaction with smooth muscle cells[15] and control the entry of immune cells into the tissue, their differentiation into specialized immune effectors as well as (co-)define their functional properties[16,17]. However, our understanding on how ECs interact with other cell types and might contribute to skeletal muscle pathology in PAD, remains largely unknown.

Macrophages are key regulators of muscle regeneration[18] but also stimulate muscle angiogenesis as well as arteriogenesis in preclinical PAD models[16,19]. The genetic and functional contribution of macrophages to skeletal muscle pathology in PAD are however unclear. Higher levels of inflammatory cytokines correlated with shorter onset claudication pain[20], but assessments of macrophage numbers and properties in skeletal muscle showed conflicting results with one manuscript showing a majority of pro-inflammatory $CD80^+$ macrophages[21], while others reported higher $CD11b^+CD206^+$ regenerative macrophages[22]

In this study, we performed a thorough transcriptomic and functional characterization of the mononuclear cell composition in skeletal muscle during PAD. We aimed to better understand the contribution of the muscle microenvironment to PAD.

52 # Results

53 ## scRNAseq reveals a high degree of cellular heterogeneity in human skeletal muscle

54 To investigate the cellular landscape of PAD patients, we collected *gastrocnemius* muscle
55 samples from individuals undergoing either PAD bypass surgery (PAD) or co-morbidity matched non-
56 ischemic individuals undergoing lower limb aneurysm surgery (non-ischemic) (see Methods, Fig. 1a,
57 Table 1). Non-ischemic patients had a normal ankle-brachial index (ABI) and no clinical symptoms of
58 PAD (no claudication symptoms, Fontaine classification = I) (Table 1). Pre-operative angiographic
59 imaging revealed that only PAD patients presented severe popliteal occlusions (GLASS grade III).

60 Myofiber size nor diameter was affected in PAD patients (Fig. 1b-d). Also, we did not observe
61 muscle necrosis but noticed a small non-significant increase in the percentage of regenerating fibers
62 (Extended Data Fig. 1a) and increased $CD31^+$ capillary (Fig. 1e-f) and arteriole densities (Extended
63 Data Fig. 1b). We next performed scRNAseq in a subset of patients (Table 1) and generated a dataset
64 comprising 106,566 cells (2359 genes/cell). Clustering revealed 9 major cell populations (Fig. 1g) that
65 we manually annotated based on the expression of well-known marker genes[23] (Fig. 1h, Fibro-
66 adipogenic progenitors (FAPs), Natural killer (NK), Monocytes/Macrophages (MoMac), Smooth
67 muscle cells (SMCs), Muscle stem cells (MuSCs)). We identified the main cell types in skeletal muscle
68 (Fig. 1g-h) and did not detect obvious differences in cell proportions between groups (Fig. 1i and
69 Extended Data Fig. 1c).

70 We additionally performed single-cell spatial transcriptomics to directly localize scRNAseq
71 populations (Table 1). We identified muscle fibers and mononuclear cells by combining transcript
72 detection with cell segmentation (Extended Data Fig. 1d) and annotated each cell through
73 integration with the scRNAseq dataset (Extended Data Fig. 1e). Approximately 75% of the detected
74 cells were fiber-derived (Extended Data Fig. 1f), reflecting the predominance of myonuclei in skeletal
75 muscle. Despite these expected differences with the scRNAseq data, ECs, FAPs and SMCs/Pericytes
76 still constituted most of the mononuclear fraction.

77 We first compared the scRNAseq patients by pseudobulk analysis, which showed different
78 transcriptomic signatures between groups (Fig. 1j and Supplementary Data 1). Gene Set Enrichment
79 Analysis (GSEA) revealed increased TNFA and IL6 signaling, as well as inflammatory activation,
80 unfolded protein response and metabolic pathways, while WNT signaling and bile acid metabolism
81 were repressed (Fig. 1k). Additionally, GSEA using a geneset collection from Human Phenotype
82 Ontology (*Abnormality of muscle physiology, HP:0011804*) revealed increased PAD-like clinical
83 symptoms while no term was enriched in non-ischemic patients (Extended Data Fig. 1g).

84 Next, we performed a comprehensive analysis on ECs, macrophages and SMCs/Pericytes
85 because of their crucial role in angiogenesis, inflammation, and tissue repair[21]. The data including all
86 identified cell populations can be interactively explored at
87 https://shiny.debocklab.hest.ethz.ch/Turiel-et-al/.

88 Human skeletal muscle contains *ATF3/4*$^{+}$ endothelial subpopulations with 89 immunoregulatory signatures

90 We selected ECs from the complete dataset and detected 6 different populations, which we
91 annotated using described marker genes[24,25] (Fig. 2a-b). Each population presented specific
92 signatures, demonstrating clustering robustness (Fig. 2c and Supplementary Data 1). We identified
93 two distinct populations of venous and capillary ECs that expressed similar markers (Fig. 2b) but
94 showed different transcriptomic signatures (Fig. 2a,c). Differential expression analysis between both
95 venous clusters detected a set of genes specifically enriched in venous 1 and capillary 1 populations
96 (Extended Data Fig. 2a). Over-representation analysis (ORA)[26] revealed that these genes are
97 associated with recruitment and functional modulation of immune cells by ECs including TNF, IL-17
98 and NF-kappa B pathways[17,27,28] as well as a lipid and atherosclerosis signaling (Fig. 2d). A deeper
99 analysis of these pathways revealed that they are involved in leukocyte recruitment and activation,
100 cell adhesion and cytokine signaling (Extended Data Fig. 2b-c). Recent studies[29] have identified
101 immunomodulatory ECs (IMECs), and the genes that define IMECs[29] were enriched in venous 1 ECs
102 (Extended Data Fig. 2d). We also observed higher expression in capillary 1 than in capillary 2
103 (Extended Data Fig. 2d, bottom panel), suggesting that both populations are ECs with
104 immunoregulatory features.

105 ORA for transcription factor (TF) motif enrichment identified c-Rel, ZNF557 and ATF4 as top
106 TFs regulating the genes enriched in both venous 1 and capillary 1 populations (Fig. 2e and Extended
107 Data Fig. 2a). We also applied SCENIC[30], which generates a *TF regulon activity score* based on the
108 coexpression of TFs and their target genes. SCENIC did not detect ZNF557 as an active TF, due to its
109 few detected target genes (intersection size in Fig. 2e), and c-Rel activity was relatively weak
110 (Extended Data Fig. 2e). In contrast, ATF4-dependent TFs factors showed high and specific activity in
111 venous 1 and capillary 1 clusters (Extended Data Fig. 2e), so we focused on *ATF3/4*. We previously
112 identified *Atf3/4*$^{+}$ muscle ECs in mouse that control exercise-induced angiogenesis[24]. The marker
113 genes defining *Atf3/4*$^{+}$ ECs were highly enriched in both venous 1 and capillary 1 human clusters
114 (Extended Data Fig. 2f). Conversely, the marker genes from the human populations (Extended Data
115 Fig. 2a) were also controlled by ATF4 in ECs (Extended Data Fig. 2g). We also used an ATF4-
116 dependent gene signature to perform gene set variation analysis (GSVA)[31] which calculates a score

117 for each cell based on the expression levels of an input gene signature. The ATF4-dependent GSVA
118 score was enriched in venous 1 and capillary 1 clusters (Fig. 2f) and we therefore annotated these
119 populations as *ATF3/4*$^+$ venous ECs and *ATF3/4*$^+$ capillary ECs. The fraction of *ATF3/4*$^+$ capillaries was
120 reduced in PAD when compared to non-ischemic samples (Fig. 2g). We also identified all EC subtypes
121 in the spatial dataset and found very consistent cluster proportions between both technologies
122 (Extended Data Fig. 2h-i).

123 We next analyzed the functional contribution of *ATF3/4*$^+$ ECs in PAD by using a preclinical
124 mouse model. We assessed muscle reperfusion following hindlimb ischemia (HLI) in wild-type (WT)
125 and EC-specific inducible ATF4 knockout mice (*Atf4*^{ECKO}). HLI efficiently reduced blood flow in both
126 genotypes leading to similar levels of ischemia-induced damage 3 days after surgery (Extended Data
127 Fig. 3a,b), characterized by large degenerative areas with cell infiltration and regenerating fibers.
128 *Atf4*^{ECKO} mice exhibited impaired blood flow recovery starting 7 days after HLI (Extended Data Fig.
129 3c,d), which coincided with reduced vessel diameter and density (Extended Data Fig. 3e-g) and lower
130 EC proliferation (Extended Data Fig. 3h). As a result, *Atf4*^{ECKO} mice showed larger damaged muscles 7
131 and 14 days after surgery (Extended Data Fig. 3a,b), illustrating the functional importance of *ATF3/4*$^+$
132 ECs to ischemia-induced revascularization in a preclinical model of PAD.

133 ECs undergo profound transcriptomic rewiring during PAD

134 Next, we assessed the transcriptional differences between conditions by calculating the
135 number of differentially expressed genes (DEGs) that are specific for each EC population (Fig. 2h and
136 Supplementary Data 1). *ATF3/4*$^+$ venous and *ATF3/4*$^+$ capillary ECs showed the highest number of
137 DEGs between non-ischemic and PAD samples (Fig. 2i). ORA on the DEGs in *ATF3/4*$^+$ venous or
138 *ATF3/4*$^+$ capillary ECs (Extended Data Fig. 4a and Supplementary Data 1) revealed that few enriched
139 processes were activated in PAD (Extended Data Fig. 4b and Supplementary Data 1), while most of
140 them were downregulated indicating that many functions exerted by these populations are
141 repressed, including angiogenesis, immune regulation, leukocyte interactions as well as metabolism
142 (Fig. 2j and Extended Data Fig. 4c). Conversely, few gene sets related to epithelial-to-mesenchymal
143 transition (EMT), platelet activation, wound healing, and cellular responses to metal ions were
144 activated in PAD (Fig. 2j).

145 The activation of EMT in *ATF3/4*$^+$ capillary ECs (Fig. 2j) prompted us to EndoMT. Focusing on
146 capillary ECs, we noticed EndoMT features[32], including repressed fatty acid metabolism genes and
147 partial mesenchymal activation (Fig. 2k). Some 'canonical' EndoMT genes like *SNAI1, S100A4* and
148 *SERPINE1* were not affected in PAD while several extracellular matrix (ECM) components, such as
149 *COL1A1*, *COL1A2* and *FN1* were highly upregulated (Fig. 2k). This phenotype was present in both

150 capillary subpopulations and they also lowered *CDH5* expression but did not completely lose it
151 (Extended Data Fig. 4d), suggesting partial EndoMT. We then investigated how ECs rewire their
152 matrisome, a set of genes that define ECM composition and function[33]. Capillary ECs in PAD only
153 changed 11.7% (32/274) of the core matrisome genes but showed significant activation of ECM
154 components such as collagens, *FN1, FBN1,* as well as alterations in components of the basement
155 membrane such as laminins, *HSPG2*, and *NID2* (Fig. 2l). Immunohistological analysis confirmed
156 increased expression of the mesenchymal marker fibronectin (FN1) by $CD31^+$ ECs in PAD (Extended
157 Data Fig. 4e,f). Taken together, ECs in PAD undergo profound transcriptomic alterations that impair
158 angiogenesis and immunoregulatory functions but promote EndoMT.

159 Finally, we used DEGs between PAD and non-ischemic ECs to predict drugs[34] that can reverse
160 the PAD EC phenotype. This analysis predicted a set of compounds with this therapeutic potential
161 (Fig. 3a), including withaferin-a or saracatinib, drugs that target inflammation and endothelial
162 dysfunction[35,36]. We focused on celastrol for its ability to improve vascular remodeling and to reduce
163 endothelial dysfunction[37]. We treated primary isolated muscle ECs (Extended Data Fig. 4g, see
164 Methods) from 3 PAD patients for 24h with vehicle (DMSO) or celastrol (125 or 250 nM[38]). RNAseq
165 analysis showed a dose-dependent effect across patients (Fig. 3b-c and Supplementary Data 1),
166 including upregulated (C1 in Fig. 3c) and downregulated genes (C2 and C3). ORA (Fig. 3d) confirmed
167 celastrol-dependent upregulation of processes related to cellular homeostasis, detoxification and
168 response to metal ions (C1) while downregulating EMT, response to wounding (C2), leukocyte
169 migration and inflammation (C2 and C3), indicating the ability of celastrol to partially reverse the PAD
170 phenotype observed in the scRNAseq dataset (Fig. 2j). Celastrol also activated ATF4 or glucosamine
171 signatures (Fig. 3e), which improves perfusion recovery in PAD preclinical models by activating
172 ATF4[39]. These findings suggest the potential of our dataset for identifying compounds that could
173 potentially revert PAD phenotypes.

174 *LYVE1*^{hi}MHCII^{low} macrophages are the dominant macrophage population in PAD

175 In experimental PAD models, monocyte-derived macrophages contribute to
176 vascularization[16,19,21,40–42]. However, acute mouse models do not reflect chronic scenarios, so the
177 contribution of macrophages to human PAD is poorly understood. We decided to further investigate
178 the Monocytes/Macrophages cluster (MoMac), selecting these cells from the complete dataset
179 where we identified and annotated 5 distinct populations[43,44] (Fig. 4a-c and Supplementary Data 1).
180 This dataset included classical monocytes (cMonocytes), *CD16*(*FCGR3A*)$^+$ monocytes, dendritic cells
181 (DCs) and two macrophage populations. Alternatively, we could also classify the populations as
182 *CCR2*$^+$*CX3CR1*^{low}*CD14*^{hi}*CD16*^{low} (cMonocytes and DCs) and *CCR2*$^-$*CX3CR1*^{hi}*CD14*^{low}*CD16*^{hi} (*CD16*$^+$
183 Monocytes)(Extended Data Fig. 5a).

184 Macrophage subpopulations were annotated as *LYVE1*^{hi}MHCII^{low}*CX3CR1*^{low} and
185 *LYVE1*^{low}MHCII^{hi}*CX3CR1*^{hi} (Extended Data Fig. 5b), matching previous characterization[45]. In mouse,
186 *LYVE1*^{hi}MHCII^{low} macrophages often have a perivascular location and a distinct ontology, phenotype
187 and function compared to monocyte-derived macrophages[45]. *LYVE1*^{hi}MHCII^{low} macrophages in our
188 dataset expressed high levels of tissue-resident macrophage markers including *LYVE1*, *FOLR2*, *CD209*,
189 *MERTK*, *SELENOP*, *STAB1* and *MAF*[44,46,47] (Fig. 4b). *LYVE1*^{hi} macrophages were the largest macrophage
190 population, even though their percentage was lower in PAD (70±6% and 40±3%, respectively, Fig.
191 4d). LYVE1/CD68 co-staining confirmed the predominance of *LYVE1*^{hi} macrophages in both conditions
192 (Fig. 4e,f), despite a significant increase in CD68^{+} monocyte/macrophages in PAD muscle (Fig. 4g),
193 consistent with previous work[21]. The spatial dataset also showed *LYVE1*^{hi} macrophages as the main
194 MoMac population in human muscle (Supplementary Fig. 5c). Notably, the percentage of *LYVE1*$^{+}$
195 macrophages over the total fraction of MoMac cells (CD68^{+}) was similar in both spatial and
196 immunofluorescence approaches (≈80-85%, Extended Data Fig. 5c and Fig. 4f) and was not affected
197 in PAD in none of them. Since the scRNAseq dataset could include (due to residual blood in the
198 sample) circulating MoMac populations such as cMonocytes and DCs, the proportional reduction in
199 *LYVE1*$^{+}$ macrophages was likely secondary to increased presence of those populations in PAD (Fig.
200 4d). Moreover, the increase of cMonocytes (Fig. 4d), but not monocyte-derived *LYVE1*^{low}MHCII^{hi}
201 macrophages, suggests impaired monocyte-to-macrophage differentiation in PAD, which was
202 confirmed using ORA (Extended Data Fig. 5d), or could be secondary to increased cMonocyte
203 numbers (Fig. 4d).

204 To evaluate whether perivascular *LYVE1*^{hi} macrophages[45] preferentially localize to specific
205 vessels, we calculated a proximity score using spatial transcriptomics, defined as the ratio of
206 observed versus expected *LYVE1*^{hi}MHCII^{low} macrophages closest to a given EC subtype. A score >1
207 indicates that *LYVE1*^{hi}MHCII^{low} macrophages are usually closer to a specific EC subtype than expected
208 by chance. In non-ischemic samples, we did not observe any spatial enrichment of *LYVE1*^{hi}MHCII^{low}
209 macrophages (Fig 4h). However, in PAD, they exhibited a significant proximity score to *ATF3/4*$^{+}$
210 Venous (Fig. 4h), indicating a preferential localization to these ECs.

211 MoMacs exert many functions depending on the biological context. Sanin et al[48] categorized
212 macrophage activation into four functional pathways: phagocytic, oxidative stress, inflammatory and
213 remodeling (regenerative). We utilized this framework to characterize the functional differences
214 between the MoMac populations in our dataset. *CD16*$^{+}$ Monocytes, cMonocytes and DCs were
215 characterized by processes related to early stage activation (ECM/cytoskeleton regulation) and
216 inflammatory/oxidative paths (innate immune response and phagosome) (Fig. 4i). *LYVE1*^{low}
217 macrophages and DCs, showed a profile of antigen presentation, consistent with their higher MHCII

218 levels (Extended Data Fig. 5b) and with their previous characterization[45]. Both *LYVE1*^{hi} and *LYVE1*^{low}
219 macrophages were characterized by a specific phagocytic profile as they were enriched in processes
220 related to complement signaling, phagocytosis and regulation of leukocyte differentiation.

221 The differential and overlapping functions of *LYVE1*^{hi} versus *LYVE1*^{low} macrophages upon loss
222 of muscle homeostasis, including PAD, are poorly understood, so we explored whether they present
223 pro-inflammatory (M1) or anti-inflammatory, pro-regenerative (M2)[49] macrophage signatures. We
224 used published genesets associated with M1 or M2 macrophages[50] under *in vitro* stimulation as well
225 as *in vivo* states of macrophages isolated from cardiotoxin-injured muscles (Ly6C^{+} macrophages at
226 day 2 after injury (pro-inflammatory) and Ly6C^{-} at day 4 after injury (pro-regenerative)). *LYVE1*^{hi}
227 macrophages expressed lower levels of both M1/inflammatory and M2/regenerative signatures (Fig.
228 4j), consistent with their proposed 'homeostatic' function. Additionally, *LYVE1*^{low} macrophages
229 showed higher expression of both signatures, although they exhibited a more pronounced pro-
230 inflammatory signature (Fig. 4j). Thus, *LYVE1*^{hi} macrophages do not reflect the genetic fingerprint of
231 M1/inflammatory nor M2/regenerative macrophages.

232 *LYVE1*^{hi}MHCII^{low} macrophages get activated during PAD

233 To assess whether MoMac populations are altered upon PAD, we detected DEGs for every
234 individual population and observed alterations across all MoMac populations (Fig. 4k,l and
235 Supplementary Data 1). Although cMonocytes showed the highest number of DEGs, most of their
236 biological processes were downregulated in PAD, including terms related to leukocyte/macrophage
237 differentiation (Extended Data Fig. 5d). Since *LYVE1*^{hi}MHCII^{low} macrophages are the dominant
238 population, and their role in muscle is poorly understood, we focused on those. Most DEGs in
239 *LYVE1*^{hi}MHCII^{low} macrophages were upregulated during PAD (Extended Data Fig. 5e and
240 Supplementary Data 1) and associated to inflammatory and immune responses, cytokine production
241 and macrophage activation (Extended Data Fig. 5f-g and Supplementary Data 1). The top repressed
242 processes in PAD were related to heat responses and protein folding (Extended Data Fig. 5g)
243 including genes such as *HSPA1A* and *HSPA1B,* which have been associated with atheroprotective and
244 anti-inflammatory roles in macrophages[51,52]. Altogether, *LYVE1*^{hi}MHCII^{low} macrophages get activated
245 and acquire pro-inflammatory properties during PAD.

246 Disruption of cellular communication networks in the muscle microenvironment
247 during PAD

248 To study cell-cell communication, we applied CellChat[53] to the complete scRNAseq dataset.
249 During PAD, the number of interactions slightly increased (Fig. 5a), although the strength of these

250 interactions was generally reduced (Fig. 5b). The increased number of interactions was mainly
251 mediated by ECs, SMcs/Pericytes, FAPs and MuSCs (Fig. 5c). Only neutrophils showed an increase in
252 interaction strength with MoMac populations during PAD (Fig. 5d). FAPs were the main signal
253 senders in the non-ischemic muscle microenvironment whereas MoMac populations were the main
254 receptors (Fig. 5e). In PAD, most populations reduced their interaction strength (Fig. 5e), suggesting
255 disrupted communication in the PAD muscle microenvironment. Indeed, most pathways were
256 reduced in PAD (Fig. 5f). MHC-II signaling was one of the top reduced communications (Fig. 5f) with
257 MoMac and ECs as they main cell types involved (Extended Data Fig. 6a). ECs reduced VEGF signaling
258 in PAD (Extended Data Fig. 6b). MuSCs showed reduced NCAM, a cell adhesion molecule that marks
259 MuSCs, interactions with FAPs (Extended Data Fig. 6c). ECs and *LYVE1*$^{+}$ macrophages reduced PDGF
260 signaling with FAPs (Extended Data Fig. 6d), a pathway involved in muscle hypertrophy and
261 regeneration[54]. *ATF3/4*$^{+}$ Venous showed reduced TRAIL signaling (Extended Data Fig. 6e), a key
262 mediator in generating stable vessels in preclinical PAD models[55]. ECs also reduced interactions of
263 several tight and adherens junctional genes including JAM, ESAM and CDH5 (Extended Data Fig. 6f-h).
264 On the other hand, pro-inflammatory IL1 and IL6 were enriched in PAD, with the latter being
265 specifically produced by *ATF3/4*$^{+}$ Venous ECs (Extended Data Fig. 6i,j). All detected interactions and
266 ligand-receptor pairs are available in Supplementary Data 1.

267 Altered SMC/Pericyte-Endothelium interactions suggest impaired vessel 268 homeostasis during PAD

269 SMCs/Pericytes are essential for proper vessel function and stability. We therefore
270 investigated how they interact with ECs during PAD. First, we annotated them based on well-known
271 marker genes of both populations[56] (Fig. 6a). Although they were present in similar proportions in
272 non-ischemic samples (Fig. 6b), SMCs comprised around 75% of mural cells in PAD. Most DEGs were
273 downregulated during PAD (Fig. 6c and Supplementary Data 1) but they increased pathways related
274 to muscle development and contractility (Fig. 6d,e) while downregulating blood vessel and
275 vasculature development processes.

276 CellChat to study capillary-pericyte and artery/venous-SMC interactions revealed that ECs
277 mainly increased FN1 signaling to both pericytes and SMCs populations (Fig. 6f), while capillaries and
278 arteries reduced PDGFB-PDGFRB and JAG2/DLL4-NOTCH3 signaling, key mediators of recruitment
279 and attachment to the endothelium[57,58]. Conversely, SMCs/Pericytes increased NAMPT signaling to
280 ECs during PAD (Fig. 6g) but reduced THBS4 (pericytes) and *PTN*, *CCL2* and *ANGPTL4* (SMCs)
281 communication (Fig. 6g). Together, these changes suggest a reduced capacity of SMC/Pericytes to
282 maintain vessel homeostasis and endothelial attachment in PAD.

Endothelial-macrophage crosstalk alters signaling networks driving inflammation and immune modulation in *LYVE*^{hi}MHCII^{low} macrophages during PAD

Finally, we analyzed EC-MoMac reciprocal communication, including Neutrophils due to their increased interaction strength with MoMacs during PAD (Fig. 5d). ECs upregulated FN1 interactions with all MoMacs while reducing MHCII signaling (Extended Data Fig. 7a). MoMacs increased *NAMPT*, linked to pro-inflammatory markers in CAD patients[59], and *THBS1* (cMonocyte-specific) signaling, elevated in PAD patients and with anti-angiogenic effects in ECs[60]. Conversely, they downregulated *VEGFA* and *ANXA1* signaling (important for inflammatory resolution in muscle[61]) with ECs and Neutrophils, respectively (Extended Data Fig. 7b). Neutrophils upregulated *NAMPT* and *OSM*, a cytokine promoting EC inflammation and neutrophil recruitment[62,63], while downregulating MHCII genes and *ANXA1*, further suggesting impaired inflammatory resolution (Extended Data Fig. 7c).

Next, we applied NicheNet[64], which can additionally link ligand-receptor pairs to their downstream signaling networks, to further study EC-macrophage interactions in PAD. Since *ATF3/4*$^{+}$ ECs present an immunomodulatory profile, and *ATF3/4*$^{+}$ Venous were the closest to *LYVE1*^{hi}MHCII^{low} macrophages in PAD (Fig. 4h), we focused on the communication between those populations. NicheNet identified different ligand-receptor pairs specifically downregulated (Fig. 7a) or upregulated (Fig. 7b) in PAD samples, indicating a profound rewiring of the communication network between *ATF3/4*$^{+}$ ECs and *LYVE1*^{hi}MHCII^{low} macrophages. Some of the top reduced signals during PAD were related to *GAS6* and *CSF1* signaling (Fig. 7a), while *IL6* signaling was enriched (Fig. 7b). We also used NicheNet to detect which upregulated genes in *LYVE1*^{hi}MHCII^{low} macrophages during PAD could be downstream targets of ligands produced by *ATF3/4*$^{+}$ ECs (Fig. 7c). These target genes included *CCL18*, *SGK1*, *PLAUR*, *CCL3*, *LMNA*, *HBEGF*, *IGFS6*, *FTH1* and *CTSB* (Fig. 7c) and are associated with migration, cytokine response, inflammatory response, and immune related processes (Fig. 7d).

To explore the ability of ECs to influence *in vitro* monocyte to macrophage differentiation in PAD, we generated conditioned media (CM) from primary muscle ECs from non-ischemic (n=3) and PAD patients (n=5) and exposed it to CD14^{+} blood cells from healthy donors (n=6). FACS analysis showed that PAD-derived CM reduced CD206 expression (M2/regenerative) while increasing CD80 and HLA-DR (M1/inflammatory) in CD14^{+} cells (Fig. 7e), indicating that PAD EC-derived factors skew CD14^{+} cells toward a pro-inflammatory profile. Although these experiments used blood CD14^{+} cells rather than specific subtypes from our scRNAseq dataset, they provide supportive evidence that altered crosstalk in muscle ECs during PAD could influence immune cell behavior.

315 ## Discussion

316 We generated a comprehensive scRNAseq dataset with over 100'000 cells from the muscle
317 microenvironment of patients with PAD as well as non-ischemic co-morbidity matched controls
318 (undergoing bypass surgery for an aneurysm). Pseudobulk analysis revealed increased TNFA and IL6
319 signaling, both associated with walking impairments in PAD patients[65,66]. Other upregulated
320 processes such as inflammation, unfolded protein response and metabolism were also reported in
321 previously bulk RNAseq studies of PAD muscle[67,68]. In contrast to our approach, those bulk studies are
322 dominated by myonuclear transcripts, suggesting common pathway alterations across cell types. Our
323 dataset provides a resource for cell-type-specific analysis of transcriptomics changes in PAD. While
324 here we focused on specific cell types, other cell (sub)populations may also critically contribute to
325 PAD progression.

326 Besides identifying common EC subpopulations, we also found *ATF3/4*$^+$ venous and capillary
327 ECs in human skeletal muscle, confirming earlier work in mice which showed that ATF3/4$^+$ ECs are
328 functionally required for exercise-induced angiogenesis[24]. A venous population, transcriptionally
329 equivalent to *ATF3/4*$^+$ venous, is specifically enriched in human skeletal muscle, adipose tissue and
330 lymph nodes[69]. Also, glucosamine-driven stimulation of ATF4 signalling improves perfusion recovery
331 in preclinical models of PAD[39]. Using this preclinical model, we showed that ATF4 deletion in ECs
332 prevents ischemia recovery, further underscoring the critical contribution of ATF4 in ECs. Our
333 scRNAseq and spatial data revealed fewer *ATF3/4*$^+$ ECs in PAD, while also reducing their angiogenic
334 and immune regulatory pathways. ECs in PAD upregulated genes related to EndoMT and cellular
335 responses to metal ions. Elevated levels of these ions have been described in patients with PAD and
336 atherosclerotic lesions[70–73], and have been linked to endothelial dysfunction[74,75]. These results
337 suggest that ECs undergo maladaptive adaptations that impair their functions in PAD. Through *in-*
338 *silico* drug repurposing, we identified celastrol as a promising candidate to reprogram PAD ECs
339 toward a healthier phenotype which highlights the potential of our scRNAseq data for therapeutic
340 discovery.

341 Blood vessel formation and remodeling is heavily influenced by resident and recruited cells.
342 In experimental models of PAD, monocyte-derived macrophages play a role in
343 vascularization[16,19,21,40–42] and muscle repair. After acute muscle ischemia or injury, macrophages
344 adopt a pro-inflammatory/M1-like phenotype. Rapidly thereafter, M1 macrophages repolarize to
345 anti-inflammatory (regenerative)/M2-like phenotype[76,77], which is required for optimal muscle
346 regeneration[77–79]. M2-like macrophages also have an important pro-angiogenic role since they are a
347 source of VEGF. Nonetheless, acute mouse models differ from chronic PAD, so the contribution of
348 macrophages in PAD remains unclear. We measured an almost 2-fold increase in CD68$^+$ cells,

349 predominantly *LYVE1*^{hi} macrophages and not monocyte-derived *LYVE1*^{low} macrophages. This
350 observation is interesting since preclinical mouse models for muscle ischemia have unequivocally
351 supported the requirement of monocyte-derived macrophages for muscle regeneration[80,81]. It is
352 unclear whether the failed accumulation of these cells in PAD patients is a result of the chronic
353 nature of PAD or contributing to the impaired regenerative response.

354 *LYVE1*^{hi}MHCII^{low} macrophages were the dominant muscle macrophage population, even
355 under a setting of chronic inflammation such as PAD. These cells were previously identified as
356 embryonically-derived, locally self-renewing tissue resident macrophages[44,82]. They cloak
357 microlesions to prevent widespread neutrophil recruitment[83] or clear damage-induced apoptotic
358 cells[47], but their contribution to PAD muscle pathology is not known. Consistent with mouse
359 literature, *LYVE1*^{hi}MHCII^{low} macrophages in our human muscle samples expressed tissue-resident
360 markers including *FOLR2* and other M2/regenerative marker genes such as *CD163* and *MRC1*
361 (CD206). However, during PAD, *LYVE1*^{hi}MHCII^{low} macrophages also activated a pro-inflammatory gene
362 program. The co-expression of genes that are typically associated with an M1 as well as M2-like state
363 might explain the contrasting findings reported in literature. Recently, TIMD4 was proposed as a
364 marker for resident mouse muscle macrophages, but we could not detect *TIMD4* expression in
365 human macrophages. Also, we found that *LYVE1*^{hi}MHCII^{low} macrophages preferentially localize close
366 to *ATF3/4*$^{+}$ ECs in PAD and showed altered (more pro-inflammatory) crosstalk with ECs. Whether
367 these altered EC-macrophage communication drives PAD muscle pathology or reflects a failed
368 homeostatic response still needs further research.

369 Analysis of the transcriptomic changes in microvascular capillary ECs revealed partial EndoMT
370 in PAD. EndoMT has been observed in atherosclerotic[84] and PAD patients[5], and ischemia promotes
371 the activation of EndoMT in several pathological settings[85]. Also, partial EndoMT is required for
372 optimal angiogenesis in myocardial infarction[32]. It is possible that persistent hypoxia contributed to a
373 partial, and chronic EndoMT. While we did observe activation of some, but not all, markers of
374 EndoMT in PAD capillary ECs, ECM genes were significantly activated. Also, the endothelial marker
375 *CDH5* was reduced, but not lost, in PAD. Interestingly, this state of partial EndoMT might be
376 reversible[32].

377 We detected strong cellular crosstalk between different cell types that was significantly
378 altered in PAD, with downregulated signaling networks related to muscle regeneration, angiogenesis
379 and vessel junctions and upregulated pro-inflammatory pathways such as *IL1B* or *IL6*. IL1B is a known
380 regulator of EndoMT[86], and IL1B inhibitors improved maximum and pain-free walking distance in
381 patients with symptomatic PAD[87], although muscle pathology was not further investigated in this
382 study. Analyzing SMCs/Pericytes-EC interactions revealed a reduction in *PGDFRB* and *NOTCH3*

383 signaling in PAD, which control mural cells recruitment and attachment to the endothelium. Also,
384 mural cells increased *NAMPT* signaling, which is associated with pro-inflammatory markers in CAD
385 patients[59]. Both SMCs and pericytes upregulated contractility genes such as *ACTA2*, *TAGLN*, *MYH11*
386 and *CNN1*, in line with increased contraction of vessels by pericytes under ischemia[88,89].This
387 phenotype might contribute to reduced perfusion in pathologies such as PAD[90]. Finally, we found
388 that LYVE1^{hi}MHCII^{low} macrophage activation could be EC-dependent. During PAD, ECs reduced *CSF1*
389 and *GAS6* signaling with LYVE1^{hi}MHCII^{low} macrophages. CSF1 is the primary growth factor responsible
390 for macrophage differentiation and survival[91], and endothelial CSF1 contributes to this[92]. Inhibition of
391 GAS6 signaling in macrophages increases their inflammatory responses[93], which would be consistent
392 with the activated state of *LYVE1*^{hi}MHCII^{low} macrophages and their increased cytokine production
393 (Extended Data Fig. 5g). The EC ligands upregulated in PAD furthermore seem to control downstream
394 genes in *LYVE1*^{hi}MHCII^{low} macrophages related to inflammation, migration and cytokine response.
395 We experimentally showed that secreted factors from ECs during PAD increased the expression of
396 M1 markers while reducing M2 markers in human CD14^{+} immune cells, further supporting a more
397 pro-inflammatory profile of ECs during PAD. Beyond having a perivascular localization, these data
398 imply that ECs might control the fate of *LYVE1*^{hi}MHCII^{low} macrophages, an exciting hypothesis that
399 requires further investigation.

400 Our study has limitations. We included a non-ischemic control group with similar
401 demographic and clinical risk factors as PAD patients to ensure that we detect PAD-specific
402 differences rather than co-morbidity related effects. Patients with aneurysms have a similar clinical
403 background of hypertension and hyperlipidemia, and a similar treatment of statins, anti-platelet
404 therapy and antihypertensive drugs (Table 1). The non-ischemic patients had a normal ABI, did not
405 show claudication symptoms during the walking test, therefore excluding the clinical manifestation
406 of PAD, and did not show occluded vessels as reported by GLASS Stage. Additionally, popliteal
407 aneurysm patients underwent a similar surgical procedure, which allowed us to standardize sample
408 harvesting. We are confident that this strategy dissected differences between both groups as
409 evidenced by the enrichment of gene sets related to abnormal muscle physiology. This said, we
410 cannot exclude that vascular aneurysms affected the composition and genetic fingerprint of the non-
411 ischemic samples. Our patient cohort was relatively small and, therefore, may be subjected to some
412 inadvertent selection bias. Our study only included male participants, so potential sex-based
413 differences could not be assessed.

414 In conclusion, we used scRNAseq to characterize the composition and transcriptional changes
415 of the muscle microenvironment in ischemic PAD compared to non-ischemic co-morbidity matched
416 patients. We identified profound transcriptomic alterations in ECs promoting EC dysfunction features

417 (such as EndoMT) while acquiring a more pro-inflammatory phenotype. *LYVE1*^{hi}MHCII^{low}
418 macrophages are the main macrophage population in ischemic PAD muscle and get activated during
419 the disease, a phenotype that may be driven by ECs. We propose that unravelling the impaired
420 cellular crosstalk in PAD muscle could potentially offer novel targets for therapeutic intervention.

421 # Methods

422 ## Patients and study design

423 Non-ischemic and PAD patients were recruited from the Department of Angiology, Cantonal
424 Hospital Baden, Baden, Switzerland. The general **inclusion criteria for both non-ischemic and PAD**
425 **patients** were: scheduled for surgery (bypass surgery in PAD patients or lower limb aneurysm surgery
426 in non-ischemic samples); Age ≥45 years; ability to understand German; signed informed consent to
427 participate in the study and received no compensation. **Inclusion criteria specific for PAD patients**:
428 diagnosis of PAD ranging from exercised limited claudication (Fontaine classification: IIa or IIb) to CLI
429 (Fontaine III-IV); ankle-brachial index (ABI) ≤ 0.90 at rest unless diagnosed with media sclerosis;
430 stable medicament regimen (i.e., statin, anti-platelet, anti-hypertensive regimen). **Inclusion criteria**
431 **specific for non-ischemic patients**: diagnosis lower limb aneurysm; ABI > 1 at rest. The general
432 **exclusion criteria for both non-ischemic and PAD patients** were: severe peripheral neuropathy
433 (Total Neuropathy Score ≥3); unstable angina or severe (>70%) three coronary vessel disease;
434 significant liver dysfunction (Model for End-Stage Liver Disease Score) or known liver cirrhosis (Child-
435 Turcotte-Pugh score >6 points); treated for cancer in the last 2 years; diagnosis of Parkinson's
436 disease. **Exclusion criteria specific for PAD patients**: above/below-knee amputation. **Exclusion**
437 **criteria specific for non-ischemic patients**: peripheral artery disease diagnosed as described before
438 (inclusion criteria specific for PAD patients). GLASS Stage: preoperative angiographic imaging (iodine
439 contrast CT angiography or digital subtraction angiography) was performed. Then, for GLASS Stage
440 calculation, the target arterial path (TAP) was identified and the femoropopliteal (FP) GLASS grade
441 (NA, I, II, III) and the infrapopliteal (IP) GLASS grade (NA, I, II, III) were determined. FP and IP scores
442 were combined to determine the final GLASS Stage. The study was conducted according to the
443 Declaration of Helsinki, the Human Research Act (HRA) and the Human Research Ordinance (HRO)
444 and the protocol was approved by the Ethics Committee of the Canton of Zurich (KEK number: 2020-
445 01393). Remaining sample material is available upon formal request to the corresponding author
446 (katrien-debock@ethz.ch).

447 Muscle samples from the peripheral region of the medial head of *gastrocnemius* muscle (1/3
448 of the distance between the tibial plateau and the malleolus medialis) were collected during lower
449 limb aneurysm surgery (non-ischemic samples) or bypass surgery (PAD samples) and immediately
450 transferred to an ice-cold hypothermic preservation solution (HypoThermosol® FRS Preservation
451 Solution, H4416 Sigma-Aldrich) for optimal transport and conservation until further processing. From
452 4 PAD and 4 non-ischemic samples, samples were processed for scRNAseq analysis, while part of the
453 tissue was also used for histology. A set of samples (n= 11 for PAD; n= 8 for non-ischemic) was

454 embedded in optimal cutting temperature medium, frozen in liquid nitrogen-cooled isopentane and
455 stored at -80°C for histological analysis. Transversal 10-µm cryosections of the samples were
456 prepared at -20°C, air dried for ~30 min and stored at -80°C until further processing. A subset of
457 histology samples (n = 3 for PAD; n = 3 for non-ischemic) was used for CosMx single-cell spatial
458 transcriptomics (see below). A set of 8 independent samples (3 non-ischemic vs 5 PAD) was used for
459 isolation and culture of primary muscle ECs (see below).

460 Isolation of cells from human skeletal muscle for single cell RNA sequencing

461 For isolation of cells for scRNAseq, and in less than 2 hours after collection and preservation
462 in ice-cold hypothermic preservation solution (HypoThermosol® FRS Preservation Solution, H4416
463 Sigma-Aldrich), samples were minced in a petri dish on ice using scissors and a surgical blade. Minced
464 samples were transferred into a digestion buffer (4 mL digestion buffer per 100 mg of muscle)
465 containing 2 mg/ml Dispase II (D4693 Sigma-Aldrich) and 2 mg/ml Collagenase IV (17104019 Thermo
466 Fisher Scientific) in HBSS buffer (14025100 Thermo Fisher Scientific) at 37°C for 25-30 minutes, with
467 gentle shaking every 3-5 minutes. After digestion, the reaction was stopped by adding an equal
468 volume of 20% heat inactivated FBS (10500064 Thermo Fisher Scientific) 1mM EDTA (E177 VWR Life
469 Science) in HBSS (14025100 Thermo Fisher Scientific) and the suspension was passed through a 100-
470 µm cell strainer (800100 Bioswisstec) and a 40-µm cell strainer (352340 Falcon). Cell suspension was
471 centrifuged at 500 g for 5 minutes at 4°C and the supernatant discarded. The pellet was resuspended
472 in 1 mL of ACK Lysing Buffer (A1049201 Thermo Fisher Scientific) for red blood cell lysis for 2 minutes
473 at room temperature. After incubation, the reaction was stopped with 4 mL of 10% heat inactivated
474 FBS (10500064 Thermo Fisher Scientific) in HBSS buffer (14025100 Thermo Fisher Scientific). Cell
475 suspension was centrifuged at 500 g for 5 minutes at 4°C and the pellet resuspended in 0.5% BSA
476 (A1391 PanReac AppliChem) in DPBS (14190250 Thermo Fisher Scientific) containing 1mM EDTA
477 (E177 VWR Life Science) for FACS. Calcein Violet (65-0854-39 Thermo Fisher Scientific) for
478 metabolically active live cells selection was added directly to the cell suspension at 1:1000 dilution 10
479 minutes before sorting.

480 Human scRNAseq analysis

481 Metabolically active (Calcein^{+}) human muscle mononuclear cells were FACS sorted and
482 loaded into the 10X Chromium Next GEM Chip G, aiming the recovery of ~10000 cells per sample.
483 scRNAseq libraries were generated according to 10X Chromium Next Gem Single Cell 3' Reagent Kits
484 v3.1 (CG000204 Rev D) and sequenced on the Illumina Novaseq 6000 system. We sequenced a total
485 of 13 samples from 8 different patients (Table 1). Sequencing reads were aligned to the human

genome using CellRanger v5.0.0-7.0.0 and the genome assembly GENCODE GRCh38.p13 Annotation Release 37. Intron reads were not included during the alignment. Each individual sample was independently processed for quality control (QC) and log-normalization using *scran* 1.24.1 and *scater* 1.24.0 packages in R (version 4.2.0). High quality cells were selected based on library size, number of detected genes and percentage of reads mapped to mitochondrial genes, independently adjusting the thresholds for each sample. Raw UMI counts were log-normalized based on library size factors. Doublets were detected and removed in every individual sample using the default parameters of the function *runDoubletFinder* from *singleCellTK* 2.6.0 package. After individual QC and log-normalization, all samples were batch-corrected and merged using *Harmony* 0.1.1 package. Dimensionality reduction by t-Distributed Stochastic Neighbor Embedding (TSNE) was performed based on the dimensions generated by *Harmony* integration. Clustering was performed by building a nearest neighbor graph (k = 20) and then applying the Louvain algorithm as implemented in *Seurat* 4.1.1 package. For individual analysis and reclustering of the EC, monocyte/macrophage and SMC/Pericytes populations, cells were selected by tracing back the clustering of the complete dataset in every individual sample. Raw counts from selected cells, either ECs, monocyte/macrophage and SMC/Pericytes were log-normalized in every individual sample and batch-corrected and merged as described above for the complete dataset. All dotplots showing gene expression were generated using the *plotDots()* function as implemented in scater 1.24.0 package. Cell type proportions in each condition were calculated by dividing the number of cells in each cluster by the total number of cells in that respective condition.

Differentially expressed genes (DEGs) were detected by performing a Wilcoxon Rank Sum test as implemented in *Seurat* 4.1.1 package. DEGs were selected based on a minimum $\log_2$ fold change of 0.25 and an adjusted p-value < 0.05. For over-representation analysis (ORA), selected DEGs were ordered based on increasing adjusted p-value and given as an input in the web-based implementation of g:Profiler[26], selecting the option "Ordered query" before running the analysis. ORA results were represented as the -log10 of the p-values obtained for each process. ORA analysis results were simplified by using *rrvgo* 1.10.0 package. Redundant terms were grouped and only the most significant term of each group was conserved. Schematic visualization of KEGG pathways from ORA results were generated using *pathview* 1.38.0 package.

For pseudobulk analysis, lowly expressed genes were removed if they were not detected in at least 10 cells. Raw UMI counts were aggregated per patient (total sum of counts for every gene from all cells in every patient). For differential expression analysis in the pseudobulk dataset, we applied *DESeq2* 1.38.3 package and performed the comparison between non-ischemic and PAD patients. All significant DEGs (adjusted p-value <0.05) were reported in a heatmap (Fig. 1j) by using the

520 normalized counts (by size factors) in each patient and scaled and centered based on gene
521 expression per patient. For Gene Set Enrichment Analysis (GSEA) in the pseudobulk dataset we
522 applied *fgsea* 1.24.0 package. From the differential expression analysis results performed with
523 DESeq2 we selected the *stat* value (Wald statistic: the log2FoldChange divided by lfcSE) for each gene
524 and performed GSEA analysis using the default settings of *fgsea()* function from *fgsea* 1.24.0
525 package. Significant pathways were selected based on an adjusted p-value < 0.05. Human Hallmark
526 pathways from MsigDB[94] were used for this analysis.

527 Gene Set Variation Analysis was performed using *GSVA* 1.46.0 package. Log-normalized
528 counts from the corresponding scRNAseq dataset (either ECs or Monocytes/Macrophages) were
529 given as an input for the *gsva()* function as implemented in GSVA 1.46.0 package. The gene sets to
530 perform GSVA were obtained from Fan et al[24] (ATF4 dependent genes as defined by genes with logFC
531 < -0.1 and adjusted p-value < 0.05 after comparing mouse muscle ECs in wild-type and EC-specific
532 inducible ATF4 knockout mice) or Sanin et al[48] (macrophage activation processes). For GSVA of M1-
533 M2 signatures, we obtained the genesets from Varga et al[50], which reported a set of M1-M2 genes
534 derived from *in vitro* stimulation and generated genesets for pro-inflammatory (Ly6C^{+}) and pro-
535 regenerative (Ly6C^{-}) macrophages at different timepoints after cardiotoxin-induced muscle injury.

536 Bulk RNAseq data from muscle ECs in WT and EC-specific ATF4 KO mice were obtained from
537 Fan et al[24] and processed as described by the authors. Only WT and ATF4 KO red muscle ECs (RmECs)
538 were used in this study.

539 Transcription factor inference analysis was performed using the Python implementation of
540 SCENIC package (pySCENIC)[30] and following the script provided by the authors in their GitHub
541 repository (https://github.com/aertslab/pySCENIC). Cell communication analysis on the complete
542 dataset (all cell types in non-ischemic and PAD samples) was performed using *CellChat* 1.6.1
543 package[53] following the script provided by the authors in their GitHub repository (*Full tutorial for*
544 *comparison analysis of multiple datasets* section in https://github.com/sqjin/CellChat). Cell
545 communication analysis between *ATF3/4*$^{+}$ ECs and *LYVE1*^{hi}MHCII^{low} macrophages was performed
546 using *nichenetr* 1.1.0 package[64] following the script provided by the authors in their GitHub
547 repository (*Differential NicheNet analysis between conditions of interest* section in
548 https://github.com/saeyslab/nichenetr).

549 All raw and processed (10X CellRanger output files) sequencing data are available at
550 GSE235143.

551 **Isolation and culture of endothelial cells from human skeletal muscle**

552 We isolated muscle ECs from 8 independent samples (3 non-ischemic vs 5 PAD) using an
553 established protocol[95], yielding high-purity (>95%) EC cultures (Extended Data Fig. 4g). As
554 recommended in the original publication[95], we performed several rounds of $CD31^+$ magnetic beads
555 sorting until we achieved the desired purity. Cells were cultured in EGM™-2 MV Microvascular
556 Endothelial Cell Growth Medium-2 BulletKit™ (CC-3202, Lonza). Subsequently, confluent EC cultures
557 from 3 PAD patients were treated for 24h with vehicle (DMSO, A994.1, Carl Roth) or celastrol (C0869,
558 Sigma-Aldrich) (125 or 250 nM), doses that are consistent with literature and do not affect cell
559 viability of HUVECs[38]. Celastrol powder was dissolved in DMSO at 2 mg/mL (stock concentration) and
560 later diluted to experimental doses (125 or 250 nM) directly into EGM-2 media right before use.
561 Control samples (Vehicle) were given the same volume of DMSO as used to dilute celastrol in the 250
562 nM condition. After 24h incubation, RNA was extracted for bulk RNA sequencing using RNeasy Plus
563 Micro Kit (74034, Qiagen) according to the manufacturer's protocol. RNA integrity was assessed by
564 using Agilent High Sensitivity RNA ScreenTape System. Only samples with RNA Integrity Number (RIN)
565 ≥ 8.0 were further processed.

566 For conditioned media experiments, confluent ECs were cultured for 48h with fresh EGM™-2
567 Medium. Then, media was collected, filtered through a 0.2 µm filter (83.1826.001, Sarstedt) and
568 cryopreserved at -80°C until further use. Cells were routinely cultured at 37°C in 21% O_2 and 5% CO_2.

569 Macrophage polarization *in vitro* using conditioned media

570 *In vitro* macrophage polarization using conditioned media was performed with an adapted
571 protocol from George et al[96]. PBMCs were obtained from buffy coats (Swiss Blood Donation Center of
572 Lugano) by density gradient centrifugation using Ficoll® Paque Plus (17-1440-02, Cytiva). $CD14^+$ cells
573 were isolated using human CD14 MicroBeads (130-050-201, Miltenyi Biotec) following the
574 manufacturer's recommendations. The purity of $CD14^+$ cells was assessed by flow cytometry (>98%,
575 except from 1 donor, >90%) (see antibodies below). $5x10^5$ $CD14^+$ cells per well were seeded in a 48-
576 well plate (TPP92148, TPP) in 250 µl of varying concentrations (0%, 6.25%, 12.5%, 25%, 50%) of
577 conditioned media (3 non-ischemic, 5 PAD). On day 3, the cells were harvested, stained for flow
578 cytometry and acquired on a BD Fortessa. The following antibodies were used: Human TruStain FcX
579 (used for Fc blocking; 422302, BioLegend), Zombie NIR™ Fixable Viability Kit (dilution 1:500, used for
580 Live/Dead staining; 423106, BioLegend), CD14 (APC-Cy7, dilution 1:200, used for purity assessment;
581 325620, BioLegend), CD19 (FITC, dilution 1:20, used for purity assessment; 555412, BD Biosciences),
582 CD3 (BV650, dilution 1:200, used for purity assessment; 300468, BioLegend), CD56 (PC5, dilution
583 1:50, used for purity assessment; A07789, Beckman Coulter), HLA-DR (BV605, dilution 1:100, used for
584 polarization assessment; 562845, BD Biosciences), CD80 (FITC, dilution 1:50, used for polarization

585 assessment; 557226, BD Biosciences), and CD206 (PE, dilution 1:50, used for polarization assessment;
586 321106, BioLegend).The data was analyzed using FlowJo v10. The experiment was performed twice
587 with $CD14^+$ cells from 3 buffy coats, respectively (total of 6 different donors).

588 Bulk RNA sequencing of celastrol-treated ECs

589 Libraries were generated using TruSeq Stranded mRNA Library Kit (Illumina) and sequenced
590 on the Illumina NovaSeq X plus. Sequencing reads were processed using Kallisto and the human
591 genome assembly GENCODE GRCh38.p13 Annotation release 42 to generate a count file matrix for
592 each individual sample. Samples were pooled together into a single matrix and analyzed following
593 DESeq2 pipeline. Differential expression analysis was performed after correcting for patient and
594 sequencing plate effect. Gene signatures for GSEA were obtained from Fan et al[24] (ATF4, see "Human
595 scRNAseq analysis" section) and Alhusban et al[39] (Glucosamine, after analyzing bulk RNAseq data
596 from original publication, HUVECs treated with glucosamine (5 mM) vs L-glucose (5 mM) for 6 hours
597 under hypoxia and serum starvation (HSS) conditions).

598 Raw and processed (Kallisto aligned) sequencing files are available at GSE287300.

599 CosMx single-cell spatial transcriptomics of muscle tissue

600 Transversal 10-µm cryosections of the samples were prepared at -20°C, air dried for ~30 min
601 and shipped to Nanostring (Seattle, WA, USA) under optimal storage conditions using dry ice to
602 ensure sample integrity. Samples were processed by Nanostring for CosMx SMI through the
603 Technology Access Program (TAP, project ID: SMI0364). For transcript detection, CosMx Human
604 Universal Cell Characterization Panel (RNA, 1000 Plex; CMX-H-USCP-1KP-R) was used. Cell detection
605 (cell segmentation) was performed using a combination of DAPI (nuclei) staining and laminin
606 staining, which marks the basal lamina surrounding individual muscle fibers to provide additional
607 structural context and facilitate accurate segmentation of mononuclear cells located between fibers.
608 Data processing was performed using Giotto package. Each sample was individually processed for
609 quality control and log-normalization and then integrated together using Harmony, following the
610 instructions from Giotto developers (https://github.com/drieslab/Giotto). To integrate spatial
611 samples with scRNAseq data and transfer cluster labels, spatial samples were treated as scRNAseq-
612 like datasets (cell-by-gene expression matrices). These were integrated with scRNAseq samples using
613 the same Harmony pipeline described in the "Human scRNAseq analysis" section. After integration,
614 all cells were projected into a shared dimensionality reduction space. We then used TSNE
615 coordinates to identify the 10 closest scRNAseq cells for each spatial cell, using Euclidean distance:

616 $\sqrt{((x_2-x_1)^2 + (y_2-y_1)^2)}$. The most frequent cluster label among the 10 nearest scRNAseq cells was
617 assigned to the corresponding spatial cell. For proximity analysis between LYVE1^{hi}MHCII^{low}
618 macrophages and EC subtypes a similar approach was followed. Briefly, after transferring cluster
619 labels to the spatial dataset, we identified the nearest EC for each LYVE^{hi}MHCII^{low} macrophage based
620 on the shortest Euclidean distance in the spatial coordinates.

621 Mice

622 Inducible EC-specific Atf4 knockout (*Pdgfb*-Cre^{ERT2} x *Atf4*$^{\Delta EC/\Delta EC}$) mice were generated as
623 described before[24]. Recombination was induced in 8-10 weeks old mice by daily intraperitoneal (IP)
624 administration of 1 mg tamoxifen (T5648, Sigma-Aldrich) dissolved in 1:10 ethanol:corn oil solution
625 for 5 consecutive days. A wash out period of at least 7 days was allowed before starting the
626 experiments. Tamoxifen-treated Cre-negative littermates were used as control for all experiments.
627 All mice were maintained on a C57BL/6N background. To label proliferating cells, an IP injection of 5-
628 ethynyl-2'-deoxyuridine (EdU) (E10187, Thermo Fischer Scientific) solution (5 mg/ml in saline) was
629 performed 7 hours before sacrificing the mice.

630 Mice were randomly allocated to different treatment groups, and the investigator was
631 blinded to the group allocation during the experiment as well as during the analysis. Mice were
632 housed at standard housing conditions (22°C, 12 h light/dark cycle), with ad libitum access to chow
633 diet (18% proteins, 4.5% fibers, 4.5% fat, 6.3% ashes, Provimi Kliba SA) and water. Health status of all
634 mice was regularly monitored according to FELASA guidelines. All animal experiments were approved
635 by the local animal ethics committee (Kantonales Veterinärsamt Zürich, license ZH050/2021), and
636 performed according to local guidelines (TschV, Zurich) and the Swiss animal protection law (TschG).
637 All mice in this study were male.

638 Hindlimb ischemia model

639 Hindlimb ischemia experiments were performed as described before[42]. Mice were
640 anesthetized with isofluorane, the hindlimbs were shaved, and, following a small incision in the skin,
641 both the proximal end of the femoral artery and the distal portion of the saphenous artery were
642 ligated. The artery and all side-branches were dissected free; after this, the femoral artery and
643 attached side-branches were excised. Immediately after surgery, perfusion was measured by Laser
644 Doppler Imaging of plantar regions of interest (Moor Instruments Ltd, Axminster, Devon, England)
645 and calculated as ratio of left (ligated) versus right (unligated) values. Perfusion was measured again
646 at different timepoints following the same procedure.

647 **Tissue Immunofluorescence and Histology**

648 Human muscles were harvested and embedded in OCT embedding matrix (6478.1, Carl Roth)
649 and frozen in liquid N_2-cooled isopentane. Frozen sections (10 µm) were made using a cryostat (Leica
650 CM 1950). The following antibodies were used: anti-LYVE1 (1:200 dilution, ab33682, Abcam), anti-
651 CD68 (1:100 dilution, ab955, Abcam), anti-CD31 (1:200 dilution, M082329-2, Dako), anti-Fibronectin
652 (1:1000 dilution, ab23750, Abcam), Goat anti-Rabbit IgG Cross-Adsorbed Secondary Antibody, Alexa
653 Fluor 568 (1:200 dilution, A-11001, Thermofisher), Goat anti-Mouse IgG Cross-Adsorbed Secondary
654 Antibody, Alexa Fluor 488 (1:200 dilution, A-1101, Thermofisher), Alexa Fluor 647 conjugated wheat
655 germ agglutinin (WGA, 1:50 dilution, W32466, ThermoFisher). Muscle sections were fixed in 4%
656 paraformaldehyde (PFA) followed by epitope retrieval using sodium citrate (10 mM, pH 6.5) at 92 °C
657 for 20 min. Endogenous peroxidase activity was blocked with 3% hydrogen peroxide in phosphate-
658 buffered saline followed by 10 min of permeabilization (PBS + 0.5% Triton X-100) and 60 min of
659 blocking at room temperature in blocking buffer (PBS + 1% BSA). After blocking, sections were
660 stained overnight at 4°C with primary antibodies, followed by 1 hour incubation of secondary
661 antibodies at room temperature. Extracellular matrix was stained using wheat germ agglutinin
662 (WGA). Nuclei were detected using Hoechst diluted 1:5000 in PBS and for 5 minutes at room
663 temperature. Slides were then washed with PBS and mounted using Immu-Mount (9990412,
664 Thermofisher). Slides were imaged on an AxioObserver.Z1 fluorescence microscope using a 20x and
665 40x objective (Carl Zeiss, Oberkochen, Germany). For the LYVE1 and CD68 staining, 315 ± 106 (mean
666 ± standard deviation [SD]) fibers were counted per patients, and for the CD31 staining, 409 ± 80
667 (mean ± SD) fibers were counted. Different regions over the whole tilescan muscle section were
668 analyzed with the Zen software (ZEN 2011 imaging software, Zeiss) and Fiji. General tissue
669 morphology was evaluated using haematoxylin and eosin (H&E) staining. H&E images were acquired
670 with an Eclipse Ti2 inverted microscope (Nikon) using a 20x objective.

671 Mouse muscles were harvested and embedded in OCT embedding matrix (6478.1, Carl Roth)
672 and frozen in liquid N_2-cooled isopentane. Frozen sections (10 µm) were made using a cryostat (Leica
673 CM 1950). For EdU detection combined with CD31, EdU was first visualized using the EdU Click-iT Cell
674 Reaction Buffer Kit (C10269, ThermoFisher) according to manufacturer's instructions, and
675 subsequently incubated for 1h in blocking buffer (PBS with 1% BSA) at room temperature.
676 Thereafter, sections were incubated overnight at 4°C with goat anti-Mouse/Rat CD31/PECAM-1
677 antibody (1:250, 3628, R&D Systems) diluted in blocking buffer with 0.1% Triton X-100.

678 **Statistics**

The histology images presented in the manuscript are representative of the data (quantification of images is approximately the group average) and the staining quality. All human imaging data are represented as violin plots, where the three horizontal lines represents the median and quartiles, and the width of the plot indicates the distribution of the data. GraphPad Prism software (version 9.2.0) was used for statistical analyses. Shapiro-Wilk test was performed to analyze data distribution. Non-normally distributed data were analyzed by non-parametric Mann-Whitney U test to compare two groups. Normally distributed data were analyzed using Student's t-test in an unpaired two-tailed fashion to compare two groups. For experiments evaluating more than one variable, a two-way ANOVA with Tukey's multiple comparison was used. For experiments evaluating more than one variable with a repeated measures design, a two-way ANOVA with Šidák's multiple comparison test was used. Each figure legend indicates the statistical approach for each experiment displayed in the figure. $p > 0.05$ is considered non-significant (ns). Asterisks in figures denote statistical significance. R and related packages were used for RNA-seq statistical analysis. Unless otherwise indicated, the default statistical test (e.g., Wilcoxon Rank Sum test for differential expression) from each package function was used. No animals or data points were excluded from the analysis.

Data availability

The RNA sequencing data underlying this article can be fully explored at https://shiny.debocklab.hest.ethz.ch/Turiel-et-al/. Additionally, raw data are available in Gene Expression Omnibus (GEO) at https://www.ncbi.nlm.nih.gov/geo/ and can be accessed with accession number GSE235143 (scRNAseq) and GSE287300 (celastrol bulk RNAseq). Processed data (scRNAseq datasets after QC, normalization, integration and clustering) can be accessed at Figshare[97] (https://doi.org/10.6084/m9.figshare.29493215).

Code availability

The following codes were used: SCENIC (https://github.com/aertslab/pySCENIC), CellChat (https://github.com/sqjin/CellChat), NicheNet (https://github.com/saeyslab/nichenetr) and Giotto (https://github.com/drieslab/Giotto). Any additional code required to reproduce the results from this manuscript is available from the corresponding author upon request (katrien-debock@ethz.ch).

Acknowledgments

The authors thank the digital trial intervention platform (dTIP) from ETH Zurich for their skilled assistance, the Functional Genomics Center Zürich (FGCZ) and the Scientific Center for Optical and Electron Microscopy (ScopeM) for excellent technical support.

This work was supported by the Swiss National Science Foundation (SNSF) [grant number 310030_208041] and Vontobel Foundation [grant number 0521/2023]. K.D.B. is endowed by the Schulthess Foundation. D.Latorre is supported by the Helmut Horten Foundation, the Novartis Foundation for medical-biological Research and the GBS/CIDP Foundation International (ETH Zurich), and the Giovanni Armenise Harvard Foundation Career Development Award (OSR, Milan).

Contributions

G.T. conceptualized the study, designed and performed the experiments and bioinformatic analyses, and wrote the paper. T.D. performed human sample processing and FACS sorting for scRNAseq. E.M. and D.Lussi performed and analyzed the histological experiments. Z.F. performed and analyzed the mouse experiments. C.M.C and D.Latorre performed and supervised the conditioned media experiments. G.B. performed the GLASS scoring. R.A., K.S., M.B. and J.Z. contributed to data analysis, interpretation, and the performance of experiments. S.F.F provided human muscle samples. S.E. conceptualized the study, recruited the patients, and performed the surgeries for human sample collection. K.D.B. conceptualized the study, supervised the experiments, acquired funding, and wrote the paper. All authors approved the final version of the paper.

Competing interests

The authors declare no competing interests.

Tables

	non-ischemic	PAD
Number of subjects	11	16
Average age (years)	73.36±2.16	73.88±2.12
Average height (cm)	175±2.04	174.69±1.78
Average weight (kg)	78.96±5.52	79.75±3.27
Average BMI	25.65±1.55	26.06±0.85
Ankle Brachial Index	1.12±0.06	0.75±0.08**
Fontaine classification I/IIa/IIb/III/IV	11/0/0/0/0	0/0/9/3/4
GLASS Stage NA/I/II/III	10/1/0/0	0/0/0/16
scRNAseq/Histology/Spatial/In vitro	4/8/3/3[†]	4/11/3/5[†]
Gender (male/female)	11/0	16/0
Smoking (never/current/former)	3/4/4	5/8/3
Obesity (BMI > 30 kg/m^2)	1 (9.1%)	2 (12.5%)
Diabetes Mellitus	3 (27.3%)	7 (43.8%)
Hypertension	9 (81.8%)	13 (81.3%)

Hyperlipidemia	8 (72.7%)	14 (87.5%)
Statins	7 (63.6%)	13 (81.3%)
Anti-platelet agents	10 (90.9%)	11 (68.8%)
Antihypertensive drugs	10 (90.9%)	12 (75.0%)
Antidiabetic agents	3 (27.3%)	7 (43.8%)
Involved side (left/right)	5/6	8/8

Table 1.Patient demographics. Continuous values are presented as mean ± standard error of the mean. BMI indicates Body Mass Index. $^{**}p < 0.01$, Student's t test (unpaired, two-tailed). †A subset of histology samples was used for scRNAseq and/or spatial experiments; In vitro experiments were performed with 3 PAD samples for bulk RNAseq and 3 vs 5 for conditioned media experiments.

Figure Legends

Fig. 1: scRNAseq reveals cell heterogeneity in PAD. a, Graphical abstract of the experimental approach used in this study. **b**, Representative images of haematoxylin and eosin (H&E)-stained sections of gastrocnemius muscle from non-ischemic (n=8) and PAD (n=11) patients (Scale bar: 50 µm). **c,d**, Quantification of fiber size in μm^2 (**c**) and minimum feret diameter in µm (**d**) from panel b. **e**, Representative images of gastrocnemius muscle from non-ischemic (n=8) and PAD (n=11) stained for the EC marker (CD31, green) and WGA (white) (Scale bar: 50 µm). **f**, Quantification of capillary density from panel e measured as the number of $CD31^+$ cells per mm^2. **g**, TSNE plot of cell populations identified from human gastrocnemius muscle, color-coded by the identified populations. **h**, Dot plot of centered logcounts values from cell type-specific marker genes. Color and size of the dots indicate the centered logcount value and the proportion of cells that express the gene, respectively. **i**, Stacked bar plots showing cluster percentage from non-ischemic (n=4) and PAD (n=4) patients, color-coded by cluster. Each stack represents mean - SEM. **j**, Heatmap of centered normalized values from top high variable genes (adjusted p-value < 0.05) in each patient based on pseudobulk analysis between non-ischemic and PAD conditions, color indicates the centered normalized values. **k**, Bar plots showing Normalized Enrichment Score of significant (adjusted p-value < 0.05) Hallmark pathways (MsigDB) from GSEA analysis on the pseudobulk dataset, color indicates the condition. Each dot represents a single patient in panels c,d and f. Student's t test (two-tailed, unpaired, parametric, ns > 0.05, $^{**}p < 0.01$) was used in c,d and f. Wald test (as implemented in DESeq2 package) was used in j. Adaptive multi-level Monte-Carlo scheme (as implemented in fgsea package) was used in k. P = 0.4535 (**c**), P = 0.4585 (**d**), P = 0.0012 (**f**). Panel **a** created with BioRender.com.

Fig. 2: Human skeletal muscle contains several EC subtypes with different functional properties. a, TSNE plot of EC subtypes identified from human gastrocnemius muscle, color-coded by the identified subtypes. **b**, Dot plot of centered logcounts values from EC subtype-specific marker genes. Color and size of the dots indicate the centered logcount value and the proportion of cells that express the gene, respectively. **c**, Heatmap of centered logcounts of DEGs (adjusted p-value <0.05) between EC subtypes, color indicates the centered logcount value. **d**,**e**, ORA analysis from genes upregulated in

761 Venous 1 compared to Venous 2 (see Extended Data Fig. 2a) using KEGG pathways (**d**) or TF motif
762 enrichment (**e**), color and size of the dots indicates the -log10 adjusted p-value and the number of
763 genes in each category (intersection size), respectively. **f**, TSNE plot of GSVA scores using the ATF4
764 dependent geneset from Fan et al (see Methods), color-coded by the GSVA score. **g**, Stacked bar
765 plots showing cluster percentage from non-ischemic (n=4) and PAD (n=4) patients, color-coded by
766 cluster. Each stack represents mean - SEM. **h**, Heatmap of centered logcounts of DEGs (adjusted p-
767 value < 0.05) specific for each EC subtype in each condition, color indicates the centered logcount
768 value. **i**, Bar plots showing the number of DEGs for each EC subtype in each condition, color indicates
769 the condition. **j**, Heatmap of centered values from ORA analysis over the DEGs in *ATF3/4*$^{+}$ venous and
770 capillary ECs between conditions, color indicates the centered values. **k,l**, Heatmap of centered
771 logcounts values of fatty acid metabolism and mesenchymal markers as defined in Tombor et al (**k**)
772 and core matrisome genes as defined in Hynes et al. (**l**), color indicates the centered values. Wilcoxon
773 Rank Sum test (as implemented in Seurat package) was used in c and h. Fisher's one-tailed test (as
774 implemented in g:Profiler) was used in d and e.

775 **Fig. 3: Celastrol partially reverses the EC PAD signature. a,** Dot plot of prediction scores (derived
776 from L1000CDS[2] search engine) from different compounds with the potential to reverse EC PAD
777 signature. Color and size of the dots indicate the rank and the prediction score, respectively. **b,**
778 Principal Component Analysis (PCA) showing sample distances between different ECs (isolated from
779 PAD patients) treated with Vehicle (DMSO) or celastrol (125 or 250 nM). Color and shape indicate
780 treatment and patient of origin, respectively. **c,** Heatmap showing centered normalized values of
781 DEGs (adjusted p-value < 0.05) between Vehicle and celastrol 250 nM, color indicates the centered
782 normalized value. Genes (rows) are organized and color-coded based on clustering of gene
783 expression profiles. **d,** ORA analysis of the gene clusters from panel c, color and size indicates
784 adjusted p-values. **e,** Bar plot (top panel) showing Normalized Enrichment Score (adjusted p-value <
785 0.05) from GSEA using ATF4 (Fan et al) and glucosamine signatures (Alhusban et al). Heatmap
786 (bottom panel) showing centered normalized values of top enriched genes from each signature, color
787 indicates the centered normalized value. Wald test (as implemented in DESeq2 package) was used in
788 c. Fisher's one-tailed test (as implemented in g:Profiler) was used in d. Adaptive multi-level Monte-
789 Carlo scheme (as implemented in fgsea package) was used in e.

790 **Fig. 4**: ***LYVE1***^{hi}**MHCII**^{low} **macrophages are the dominant macrophage population in PAD. a**, TSNE plot
791 of Monocytes/Macrophages subtypes identified from human gastrocnemius muscle, color-coded by
792 the identified subtypes. **b**, Dot plot of centered logcounts values from MoMac subtype-specific
793 marker genes. Dot color indicates centered logcounts, and size reflects the proportion of cells
794 expressing the gene. **c**, Heatmap of centered logcounts of DEGs (adjusted p-value <0.05) between

795 MoMac subtypes, color indicates the centered logcount value. **d**, Stacked bar plots showing cluster
796 percentage from non-ischemic (n=4) and PAD (n=4) patients, color-coded by cluster. Each stack
797 shows mean - SEM. **e**, Representative images of gastrocnemius muscle from non-ischemic (n=8) and
798 PAD (n=11) stained for a pan-macrophage marker (CD68, green), LYVE1 (magenta), cell nuclei
799 (Hoechst, blue) and WGA (white). Top left panel has a lower magnification compared to the other 3
800 pictures. White rectangle indicates the zoomed area displayed in the remaining panels (Scale bar: 50
801 µm). **f-g**, Quantification of the percentage of LYVE1^{+}CD68^{+} cells from the total of CD68^{+} cells (**f**) and
802 the total number of macrophages measured as the number of CD68^{+} cells/mm^{2} (**g**). **h**, Bar plot
803 showing proximity scores (see Methods) of *LYVE1*^{hi}MHCII^{low} macrophages to each EC subtype in the
804 spatial dataset from non-ischemic (n=3) and PAD (n=3) patients. Color coded by condition. Each bar
805 represents mean ± SEM. **i,** TSNE plots showing GSVA scores for different macrophage activation
806 processes as defined by Sanin et al, color-coded by GSVA score. **j**, GSVA scores from different pro-
807 inflammatory and pro-regenerative signatures as defined by Varga et al between *LYVE1*^{hi} and *LYVE*^{low}
808 macrophages, color-coded by cluster. **k**, Heatmap of centered logcounts of DEGs (adjusted p-value <
809 0.05) specific for each MoMac subtype in each condition, color indicates the centered logcount
810 value. **l**, Bar plot showing the number of DEGs for each MoMac subtype in each condition, color
811 indicates the condition. Each dot represents a single patient in panels f, g and h. Wilcoxon Rank Sum
812 test (as implemented in Seurat package) was used in c and k. Student's t test (two-tailed, unpaired,
813 parametric, ns > 0.05) was used in f and Mann-Whitney U test (two-tailed, unpaired, non-parametric,
814 $^{*}p < 0.05$). was used in g. Binomial test (one-tailed, observed vs expected, $^{*}p < 0.05$) was used in h. P
815 = 0.3511 (**f**), P = 0.0473 (**g**), P = 0.0066 (**h**, PAD Capillary), P = 0.0007 (**h**, PAD *ATF3/4*$^{+}$ Venous).

816 **Fig. 5: Cellular communication in human skeletal muscle is disrupted in PAD. a-b**, Circle plots
817 showing the number (**a**) and weight (**b**) of inferred interactions between cell types in non-ischemic
818 and PAD (left and middle plots) and bar plots quantifying these parameters (right plots). Color and
819 width of the edges indicates the sender and number or weight of interactions, respectively. **c-d**,
820 Heatmaps showing increased (red) or decreased (blue) number (**c**) and weight (**d**) of inferred
821 interactions in PAD. Labels on the left side indicate the cell type expressing the ligands and bottom
822 labels the cell types receiving them. **e**, Scatter plots showing the strength of the outgoing (x-axis) and
823 incoming (y-axis) interactions for each cell type in non-ischemic (left) and PAD (right). Color and size
824 of the dots indicate the cell type and the number of inferred interactions, respectively. **f**, Bar plots
825 showing the relative information flow for significant communication pathways between non-
826 ischemic and PAD

827 **Fig. 6: Cellular communication between mural cells and ECs indicates reduced vessel homeostasis.**
828 **a,** Dot plot of centered logcounts values from SMCs and Pericytes marker genes. Color and size of the

829 dots indicate the centered logcounts values and the proportion of cells that express the gene,
830 respectively. **b,** Stacked bar plots showing cluster percentage in each condition, color-coded by
831 cluster. Each stack represents mean – SEM. **c,** Heatmap of centered logcounts of DEGs (adjusted p-
832 value <0.05) from SMCs (top) and Pericytes (bottom) between conditions, color indicates the
833 centered logcount value. **d-e,** ORA analysis of top biological processes of DEGs from panel c in SMCs
834 (**d**) and Pericytes (**e**), color indicates in which condition the process is significant (adjusted p-value <
835 0.05). **f-g**, Circle plots of ligand and receptors up/downregulated in PAD from ECs to mural cells (**f**)
836 and from mural cells to ECs (**g**). Color and width of the edges indicates the sender and weight of
837 interactions, respectively. Wilcoxon Rank Sum test (as implemented in Seurat package) was used in c.
838 Fisher's one-tailed test (as implemented in g:Profiler) was used in d and e.

839 **Fig. 7: Cellular communication between *ATF3/4*$^{+}$ ECs and *LYVE1*^{hi}MHCII^{low} macrophages is altered**
840 **during PAD. a-b**, Heatmaps showing downregulated (**a**) and upregulated (**b**) ligand-receptor (LR)
841 pairs in PAD. In each panel, left part indicates the ligand log fold change (LFC) in *ATF3/4*$^{+}$ ECs and
842 right part the receptor LFC in *LYVE1*^{hi}MHCII^{low} macrophages from each LR pair. Color indicates the
843 LFC. **c**, Heatmap showing the regulatory potential of *ATF3/4*$^{+}$ ECs ligands upregulated in PAD (left
844 labels) over the downstream target genes upregulated in *LYVE1*^{hi}MHCII^{low} macrophages (top labels).
845 Color indicates the regulatory potential. **d**, Dot plot showing ORA results from the predicted targets
846 in panel c. Color and size of the dots indicate -log10 adjusted p-value and number of genes in each
847 category (intersection size), respectively. **e**, Graphs showing the geomean expression ± SEM of the
848 markers CD206, CD80 and HLA-DR on human CD14^{+} cells cultured *in vitro* with increasing
849 concentrations of ECs-derived conditioned media (CM). Non-ischemic CM (grey, n=3) and PAD CM
850 (blue, n=5). Fisher's one-tailed test (as implemented in g:Profiler) was used in d. Two-way ANOVA (*
851 p-value < 0.05, *** p-value < 0.001) was used in e. P = 0.0002 (**e**, CD206), P = 0.0001 (**e**, CD80), P =
852 0.0414 (**e**, HLA-DR).

853 ## References

854 1. Fowkes, F. G. R. *et al.* Peripheral artery disease: epidemiology and global perspectives. *Nat*
855 *Rev Cardiol* **14**, 156–170 (2017).

856 2. ROSE, G. A. The diagnosis of ischaemic heart pain and intermittent claudication in field
857 surveys. *Bull World Health Organ* **27**, 645–58 (1962).

858 3. Bethel, M. & Annex, B. H. Peripheral arterial disease: A small and large vessel problem.
859 *American Heart Journal Plus: Cardiology Research and Practice* **28**, 100291 (2023).

860 4. Annex, B. H. Therapeutic angiogenesis for critical limb ischaemia. *Nat Rev Cardiol* **10**, 387–396
861 (2013).

862 5. Chevalier, J. *et al.* Obstruction of Small Arterioles in Patients with Critical Limb Ischemia due to
863 Partial Endothelial-to-Mesenchymal Transition. *iScience* **23**, 101251 (2020).

864 6. Mietus, C. J. *et al.* Abnormal Microvascular Architecture, Fibrosis, and Pericyte Characteristics
865 in the Calf Muscle of Peripheral Artery Disease Patients with Claudication and Critical Limb
866 Ischemia. *J Clin Med* **9**, 2575 (2020).

867 7. Coats, P. & Hillier, C. Differential Responses in Human Subcutaneous and Skeletal Muscle
868 Vascular Beds to Critical Limb Ischaemia. *European Journal of Vascular and Endovascular*
869 *Surgery* **19**, 387–395 (2000).

870 8. Hammarsten, J., Bylund-Fellenius, A. C., Holm, J., Scherstén, T. & Krotkiewski, M. Capillary
871 supply and muscle fibre types in patients with intermittent claudication: relationships
872 between morphology and metabolism. *Eur J Clin Invest* **10**, 301–5 (1980).

873 9. Ho, T. K. *et al.* Increased endogenous angiogenic response and hypoxia-inducible factor-1α in
874 human critical limb ischemia. *J Vasc Surg* **43**, 125–133 (2006).

875 10. McGuigan, M. R. *et al.* Muscle fiber characteristics in patients with peripheral arterial disease.
876 *Med Sci Sports Exerc* **33**, 2016–21 (2001).

877 11. Tsui, J. C. S., Baker, D. M., Biecker, E., Shaw, S. & Dashwood, M. R. Potential role of endothelin
878 1 in ischaemia-induced angiogenesis in critical leg ischaemia. *Br J Surg* **89**, 741–7 (2002).

879 12. Clyne, C. A., Mears, H., Weller, R. O. & O'Donnell, T. F. Calf muscle adaptation to peripheral
880 vascular disease. *Cardiovasc Res* **19**, 507–12 (1985).

881 13. Robbins, J. L. *et al.* Relationship between leg muscle capillary density and peak hyperemic
882 blood flow with endurance capacity in peripheral artery disease. *J Appl Physiol (1985)* **111**,
883 81–6 (2011).

884 14. Christov, C. *et al.* Muscle satellite cells and endothelial cells: close neighbors and privileged
885 partners. *Mol Biol Cell* **18**, 1397–409 (2007).

886 15. Méndez-Barbero, N., Gutiérrez-Muñoz, C. & Blanco-Colio, L. Cellular Crosstalk between
887 Endothelial and Smooth Muscle Cells in Vascular Wall Remodeling. *Int J Mol Sci* **22**, 7284
888 (2021).

889 16. Krishnasamy, K. *et al.* Blood vessel control of macrophage maturation promotes
890 arteriogenesis in ischemia. *Nat Commun* **8**, 952 (2017).

891 17. Amersfoort, J., Eelen, G. & Carmeliet, P. Immunomodulation by endothelial cells — partnering
892 up with the immune system? *Nat Rev Immunol* **22**, 576–588 (2022).

893 18. Dort, J., Fabre, P., Molina, T. & Dumont, N. A. Macrophages Are Key Regulators of Stem Cells
894 during Skeletal Muscle Regeneration and Diseases. *Stem Cells Int* **2019**, 4761427 (2019).

895 19. Ganta, V. C. *et al.* A MicroRNA93–Interferon Regulatory Factor-9–Immunoresponsive Gene-1–
896 Itaconic Acid Pathway Modulates M2-Like Macrophage Polarization to Revascularize Ischemic
897 Muscle. *Circulation* **135**, 2403–2425 (2017).

898 20. Casale, G. P. *et al.* Cytokine signature of inflammation mediated by autoreactive Th-cells, in
899 calf muscle of claudicating patients with Fontaine stage II peripheral artery disease.
900 *Translational Research* **228**, 94–108 (2021).

901 21. Ganta, V. C., Choi, M., Farber, C. R. & Annex, B. H. Antiangiogenic VEGF $_{165}$ b Regulates
902 Macrophage Polarization via S100A8/S100A9 in Peripheral Artery Disease. *Circulation* **139**,
903 226–242 (2019).

904 22. Kosmac, K. *et al.* Correlations of Calf Muscle Macrophage Content With Muscle Properties and
905 Walking Performance in Peripheral Artery Disease. *J Am Heart Assoc* **9**, (2020).

906 23. Jones, R. C. *et al.* The Tabula Sapiens: A multiple-organ, single-cell transcriptomic atlas of
907 humans. *Science (1979)* **376**, (2022).

908 24. Fan, Z. *et al.* Exercise-induced angiogenesis is dependent on metabolically primed ATF3/4+
909 endothelial cells. *Cell Metab* **33**, 1793-1807.e9 (2021).

910 25. Kalucka, J. *et al.* Single-Cell Transcriptome Atlas of Murine Endothelial Cells. *Cell* **180**, 764-
911 779.e20 (2020).

912 26. Raudvere, U. *et al.* g:Profiler: a web server for functional enrichment analysis and conversions
913 of gene lists (2019 update). *Nucleic Acids Res* **47**, W191–W198 (2019).

914 27. Wedgwood, J. F., Hatam, L. & Bonagura, V. R. Effect of interferon-gamma and tumor necrosis
915 factor on the expression of class I and class II major histocompatibility molecules by cultured
916 human umbilical vein endothelial cells. *Cell Immunol* **111**, 1–9 (1988).

917 28. Mai, J. *et al.* Interleukin-17A Promotes Aortic Endothelial Cell Activation via Transcriptionally
918 and Post-translationally Activating p38 Mitogen-activated Protein Kinase (MAPK) Pathway. *J*
919 *Biol Chem* **291**, 4939–54 (2016).

920 29. Alnaqbi, H. *et al.* Immunomodulation by endothelial cells: prospects for cancer therapy.
921 *Trends Cancer* **10**, 1072–1091 (2024).

922 30. Aibar, S. *et al.* SCENIC: single-cell regulatory network inference and clustering. *Nat Methods*
923 **14**, 1083–1086 (2017).

924 31. Hänzelmann, S., Castelo, R. & Guinney, J. GSVA: gene set variation analysis for microarray and
925 RNA-Seq data. *BMC Bioinformatics* **14**, 7 (2013).

926 32. Tombor, L. S. *et al.* Single cell sequencing reveals endothelial plasticity with transient
927 mesenchymal activation after myocardial infarction. *Nat Commun* **12**, 681 (2021).

928 33. Hynes, R. O. & Naba, A. Overview of the matrisome--an inventory of extracellular matrix
929 constituents and functions. *Cold Spring Harb Perspect Biol* **4**, a004903 (2012).

930 34. Duan, Q. *et al.* L1000CDS2: LINCS L1000 characteristic direction signatures search engine. *NPJ*
931 *Syst Biol Appl* **2**, 16015 (2016).

932 35. Batumalaie, K., Amin, M. A., Murugan, D. D., Sattar, M. Z. A. & Abdullah, N. A. Withaferin A
933 protects against palmitic acid-induced endothelial insulin resistance and dysfunction through
934 suppression of oxidative stress and inflammation. *Sci Rep* **6**, 27236 (2016).

935 36. Amadori, L. *et al.* Systems immunology-based drug repurposing framework to target
936 inflammation in atherosclerosis. *Nature Cardiovascular Research* **2**, 550–571 (2023).

937 37. Tan, J.-L. *et al.* Celastrol: The new dawn in the treatment of vascular remodeling diseases.
938 *Biomedicine & Pharmacotherapy* **158**, 114177 (2023).

939 38. Li, G. *et al.* Targeting OPA1-Mediated Mitochondrial Fusion Contributed to Celastrol's Anti-
940 Tumor Angiogenesis Effect. *Pharmaceutics* **15**, 48 (2022).

941 39. Alhusban, S. *et al.* Glucosamine-Mediated Hexosamine Biosynthesis Pathway Activation Uses
942 ATF4 to Promote "Exercise-Like" Angiogenesis and Perfusion Recovery in PAD. *Circulation* **150**,
943 1702–1719 (2024).

944 40. Simons, M. & Ware, J. A. Therapeutic angiogenesis in cardiovascular disease. *Nat Rev Drug*
945 *Discov* **2**, 863–71 (2003).

946 41. Hamm, A. *et al.* PHD2 regulates arteriogenic macrophages through TIE2 signalling. *EMBO Mol*
947 *Med* **5**, 843–857 (2013).

948 42. Zhang, J. *et al.* Endothelial Lactate Controls Muscle Regeneration from Ischemia by Inducing
949 M2-like Macrophage Polarization. *Cell Metab* **31**, 1136-1153.e7 (2020).

950 43. Mulder, K. *et al.* Cross-tissue single-cell landscape of human monocytes and macrophages in
951 health and disease. *Immunity* **54**, 1883-1900.e5 (2021).

952 44. Dick, S. A. *et al.* Three tissue resident macrophage subsets coexist across organs with
953 conserved origins and life cycles. *Sci Immunol* **7**, (2022).

954 45. Chakarov, S. *et al.* Two distinct interstitial macrophage populations coexist across tissues in
955 specific subtissular niches. *Science (1979)* **363**, (2019).

956 46. Moura Silva, H. *et al.* c-MAF–dependent perivascular macrophages regulate diet-induced
957 metabolic syndrome. *Sci Immunol* **6**, (2021).

958 47. Babaeijandaghi, F. *et al.* Metabolic reprogramming of skeletal muscle by resident
959 macrophages points to CSF1R inhibitors as muscular dystrophy therapeutics. *Sci Transl Med*
960 **14**, (2022).

961 48. Sanin, D. E. *et al.* A common framework of monocyte-derived macrophage activation. *Sci*
962 *Immunol* **7**, (2022).

963 49. Martinez, F. O. & Gordon, S. The M1 and M2 paradigm of macrophage activation: time for
964 reassessment. *F1000Prime Rep* **6**, (2014).

965 50. Varga, T. *et al.* Highly Dynamic Transcriptional Signature of Distinct Macrophage Subsets
966 during Sterile Inflammation, Resolution, and Tissue Repair. *The Journal of Immunology* **196**,
967 4771–4782 (2016).

968 51. Brykczynska, U. *et al.* Distinct Transcriptional Responses across Tissue-Resident Macrophages
969 to Short-Term and Long-Term Metabolic Challenge. *Cell Rep* **30**, 1627-1643.e7 (2020).

970 52. Dulin, E., García-Barreno, P. & Guisasola, M. C. Genetic variations of HSPA1A, the heat shock
971 protein levels, and risk of atherosclerosis. *Cell Stress Chaperones* **17**, 507–16 (2012).

972 53. Jin, S. *et al.* Inference and analysis of cell-cell communication using CellChat. *Nat Commun* **12**,
973 1088 (2021).

974 54. Sugg, K. B., Korn, M. A., Sarver, D. C., Markworth, J. F. & Mendias, C. L. Inhibition of
975 platelet-derived growth factor signaling prevents muscle fiber growth during skeletal muscle
976 hypertrophy. *FEBS Lett* **591**, 801–809 (2017).

977 55. Cartland, S. P. *et al.* The generation of stable microvessels in ischemia is mediated by
978 endothelial cell derived TRAIL. *Sci Adv* **10**, (2024).

979 56. van Splunder, H., Villacampa, P., Martínez-Romero, A. & Graupera, M. Pericytes in the disease
980 spotlight. *Trends Cell Biol* **34**, 58–71 (2024).

981 57. Liu, H., Zhang, W., Kennard, S., Caldwell, R. B. & Lilly, B. Notch3 Is Critical for Proper
982 Angiogenesis and Mural Cell Investment. *Circ Res* **107**, 860–870 (2010).

983 58. Gaengel, K., Genové, G., Armulik, A. & Betsholtz, C. Endothelial-Mural Cell Signaling in
984 Vascular Development and Angiogenesis. *Arterioscler Thromb Vasc Biol* **29**, 630–638 (2009).

985 59. Halvorsen, B. *et al.* Increased expression of NAMPT in PBMC from patients with acute
986 coronary syndrome and in inflammatory M1 macrophages. *Atherosclerosis* **243**, 204–10
987 (2015).

988 60. Smadja, D. M. *et al.* Thrombospondin-1 Is a Plasmatic Marker of Peripheral Arterial Disease
989 That Modulates Endothelial Progenitor Cell Angiogenic Properties. *Arterioscler Thromb Vasc*
990 *Biol* **31**, 551–559 (2011).

991 61. McArthur, S. *et al.* Annexin A1 drives macrophage skewing to accelerate muscle regeneration
992 through AMPK activation. *Journal of Clinical Investigation* **130**, 1156–1167 (2020).

993 62. van Keulen, D. *et al.* Inflammatory cytokine oncostatin M induces endothelial activation in
994 macro- and microvascular endothelial cells and in APOE*3Leiden.CETP mice. *PLoS One* **13**,
995 e0204911 (2018).

996 63. Kerfoot, S. M. *et al.* Exclusive Neutrophil Recruitment with Oncostatin M in a Human System.
997 *Am J Pathol* **159**, 1531–1539 (2001).

998 64. Browaeys, R., Saelens, W. & Saeys, Y. NicheNet: modeling intercellular communication by
999 linking ligands to target genes. *Nat Methods* **17**, 159–162 (2020).

1000 65. Pande, R. L. *et al.* Association of monocyte tumor necrosis factor α expression and serum
1001 inflammatory biomarkers with walking impairment in peripheral artery disease. *J Vasc Surg*
1002 **61**, 155–161 (2015).

1003 66. Signorelli, S. S. *et al.* High circulating levels of cytokines (IL-6 and TNFalpha), adhesion
1004 molecules (VCAM-1 and ICAM-1) and selectins in patients with peripheral arterial disease at
1005 rest and after a treadmill test. *Vasc Med* **8**, 15–9 (2003).

1006 67. Ferrucci, L. *et al.* Transcriptomic and Proteomic of Gastrocnemius Muscle in Peripheral Artery
1007 Disease. *Circ Res* (2023) doi:10.1161/CIRCRESAHA.122.322325.

1008 68. Ryan, T. E. *et al.* Extensive skeletal muscle cell mitochondriopathy distinguishes critical limb
1009 ischemia patients from claudicants. *JCI Insight* **3**, (2018).

1010 69. Barnett, S. N. *et al.* An organotypic atlas of human vascular cells. *Nat Med* **30**, 3468–3481
1011 (2024).

1012 70. Tellez-Plaza, M. *et al.* Cadmium exposure and incident peripheral arterial disease. *Circ*
1013 *Cardiovasc Qual Outcomes* **6**, 626–33 (2013).

1014 71. Stadler, N. *et al.* Accumulation of Zinc in Human Atherosclerotic Lesions Correlates With
1015 Calcium Levels But Does Not Protect Against Protein Oxidation. *Arterioscler Thromb Vasc Biol*
1016 **28**, 1024–1030 (2008).

1017 72. Bagheri, B., Akbari, N., Tabiban, S., Habibi, V. & Mokhberi, V. Serum level of copper in patients
1018 with coronary artery disease. *Niger Med J* **56**, 39–42 (2015).

1019 73. Navas-Acien, A. *et al.* Metals in urine and peripheral arterial disease. *Environ Health Perspect*
1020 **113**, 164–9 (2005).

1021 74. Knoflach, M. *et al.* Non-toxic cadmium concentrations induce vascular inflammation and
1022 promote atherosclerosis. *Circ J* **75**, 2491–5 (2011).

1023 75. Yeh, S.-C., Tsai, F.-Y., Chao, H.-R. & Tsou, T.-C. Zinc ions induce inflammatory responses in
1024 vascular endothelial cells. *Bull Environ Contam Toxicol* **87**, 113–6 (2011).

1025 76. Mosser, D. M. & Edwards, J. P. Exploring the full spectrum of macrophage activation. *Nat Rev*
1026 *Immunol* **8**, 958–69 (2008).

1027 77. Arnold, L. *et al.* Inflammatory monocytes recruited after skeletal muscle injury switch into
1028 antiinflammatory macrophages to support myogenesis. *J Exp Med* **204**, 1057–69 (2007).

1029 78. Deng, B., Wehling-Henricks, M., Villalta, S. A., Wang, Y. & Tidball, J. G. IL-10 triggers changes in
1030 macrophage phenotype that promote muscle growth and regeneration. *J Immunol* **189**, 3669–
1031 80 (2012).

1032 79. Tidball, J. G. & Wehling-Henricks, M. Macrophages promote muscle membrane repair and
1033 muscle fibre growth and regeneration during modified muscle loading in mice in vivo. *J Physiol*
1034 **578**, 327–36 (2007).

1035 80. Vågesjö, E. *et al.* Perivascular Macrophages Regulate Blood Flow Following Tissue Damage.
1036 *Circ Res* **128**, 1694–1707 (2021).

1037 81. Lu, H. *et al.* Macrophages recruited via CCR2 produce insulin-like growth factor-1 to repair
1038 acute skeletal muscle injury. *FASEB J* **25**, 358–69 (2011).

1039 82. Wang, X. *et al.* Heterogeneous origins and functions of mouse skeletal muscle-resident
1040 macrophages. *Proceedings of the National Academy of Sciences* **117**, 20729–20740 (2020).

1041 83. Uderhardt, S., Martins, A. J., Tsang, J. S., Lämmermann, T. & Germain, R. N. Resident
1042 Macrophages Cloak Tissue Microlesions to Prevent Neutrophil-Driven Inflammatory Damage.
1043 *Cell* **177**, 541-555.e17 (2019).

1044 84. Chen, P.-Y. *et al.* Endothelial-to-mesenchymal transition drives atherosclerosis progression. *J*
1045 *Clin Invest* **125**, 4514–28 (2015).

1046 85. Manavski, Y. *et al.* Clonal Expansion of Endothelial Cells Contributes to Ischemia-Induced
1047 Neovascularization. *Circ Res* **122**, 670–677 (2018).

1048 86. Maleszewska, M. *et al.* IL-1β and TGFβ2 synergistically induce endothelial to mesenchymal
1049 transition in an NFκB-dependent manner. *Immunobiology* **218**, 443–54 (2013).

1050 87. Russell, K. S. *et al.* A randomized, placebo-controlled trial of canakinumab in patients with
1051 peripheral artery disease. *Vasc Med* **24**, 414–421 (2019).

1052 88. Methner, C. *et al.* Pericyte constriction underlies capillary derecruitment during hyperemia in
1053 the setting of arterial stenosis. *American Journal of Physiology-Heart and Circulatory*
1054 *Physiology* **317**, H255–H263 (2019).

1055 89. Alarcon-Martinez, L. *et al.* Retinal ischemia induces α-SMA-mediated capillary pericyte
1056 contraction coincident with perivascular glycogen depletion. *Acta Neuropathol Commun* **7**,
1057 134 (2019).

1058 90. Kaul, S., Methner, C. & Mishra, A. The Role of Pericytes in Hyperemia-Induced Capillary De-
1059 Recruitment Following Stenosis. *Curr Tissue Microenviron Rep* **1**, 163–169 (2020).

1060 91. Sehgal, A., Irvine, K. M. & Hume, D. A. Functions of macrophage colony-stimulating factor
1061 (CSF1) in development, homeostasis, and tissue repair. *Semin Immunol* **54**, 101509 (2021).

1062 92. Sinha, S. K. *et al.* Local M-CSF (Macrophage Colony-Stimulating Factor) Expression Regulates
1063 Macrophage Proliferation and Apoptosis in Atherosclerosis. *Arterioscler Thromb Vasc Biol* **41**,
1064 220–233 (2021).

1065 93. Deng, T., Zhang, Y., Chen, Q., Yan, K. & Han, D. Toll-like receptor-mediated inhibition of Gas6
1066 and ProS expression facilitates inflammatory cytokine production in mouse macrophages.
1067 *Immunology* **135**, 40–50 (2012).

1068 94. Liberzon, A. *et al.* The Molecular Signatures Database Hallmark Gene Set Collection. *Cell Syst*
1069 **1**, 417–425 (2015).

1070 95. Wüst, R., Terrie, L., Müntefering, T., Ruck, T. & Thorrez, L. Efficient co-isolation of
1071 microvascular endothelial cells and satellite cell-derived myoblasts from human skeletal
1072 muscle. *Front Bioeng Biotechnol* **10**, (2022).

1073 96. George, S., Georgouli, M. & Sanz-Moreno, V. Protocol to drive human monocyte-to-
1074 macrophage polarization in vitro using tumor conditioned media. *STAR Protoc* **3**, 101666
1075 (2022).

1076 97. Turiel, G. scRNAseq Seurat and SCE objects. *Figshare*
1077 https://figshare.com/articles/dataset/scRNAseq_Seurat_and_SCE_objects/29493215 (2025)
1078 doi:10.6084/m9.figshare.29493215.v1.

1079

1080

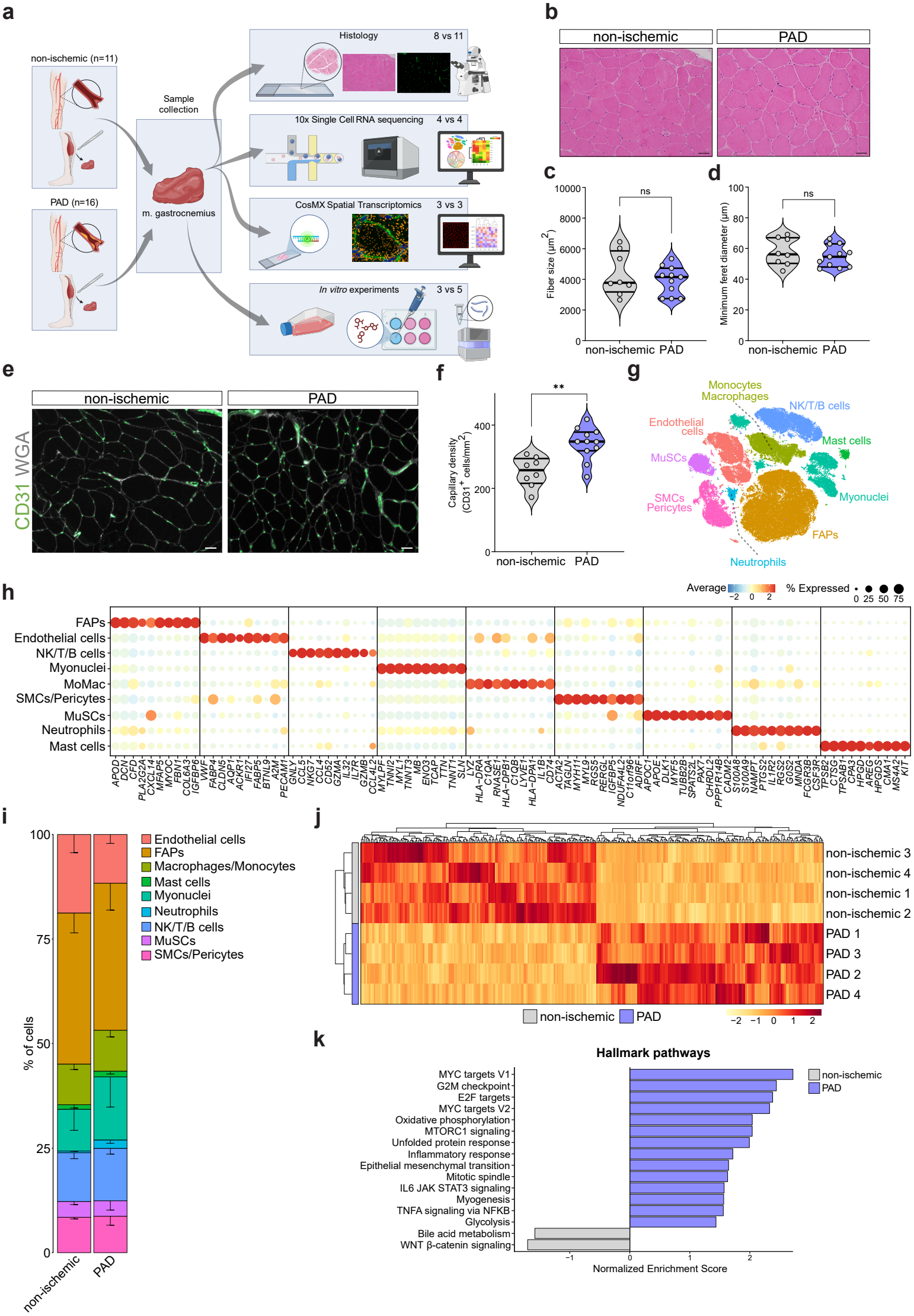
a
non-ischemic (n=11)
PAD (n=16)
Sample collection
m. gastrocnemius
Histology
8 vs 11
10x Single Cell RNA sequencing
4 vs 4
CosMX Spatial Transcriptomics
3 vs 3
In vitro experiments
3 vs 5
b
non-ischemic
PAD
c
Fiber size (µm²)
ns
non-ischemic PAD
d
Minimum feret diameter (µm)
ns
non-ischemic PAD
e
non-ischemic
PAD
CD31 WGA
f
Capillary density (CD31⁺ cells/mm²)
**
non-ischemic PAD
g
Monocytes Macrophages
NK/T/B cells
Endothelial cells
Mast cells
MuSCs
Myonuclei
SMCs Pericytes
FAPs
Neutrophils
h
Average
% Expressed
FAPs
Endothelial cells
NK/T/B cells
Myonuclei
MoMac
SMCs/Pericytes
MuSCs
Neutrophils
Mast cells
i
% of cells
Endothelial cells
FAPs
Macrophages/Monocytes
Mast cells
Myonuclei
Neutrophils
NK/T/B cells
MuSCs
SMCs/Pericytes
non-ischemic
PAD
j
non-ischemic 3
non-ischemic 4
non-ischemic 1
non-ischemic 2
PAD 1
PAD 3
PAD 2
PAD 4
non-ischemic
PAD
k
Hallmark pathways
MYC targets V1
G2M checkpoint
E2F targets
MYC targets V2
Oxidative phosphorylation
MTORC1 signaling
Unfolded protein response
Inflammatory response
Epithelial mesenchymal transition
Mitotic spindle
IL6 JAK STAT3 signaling
Myogenesis
TNFA signaling via NFKB
Glycolysis
Bile acid metabolism
WNT β-catenin signaling
Normalized Enrichment Score
non-ischemic
PAD

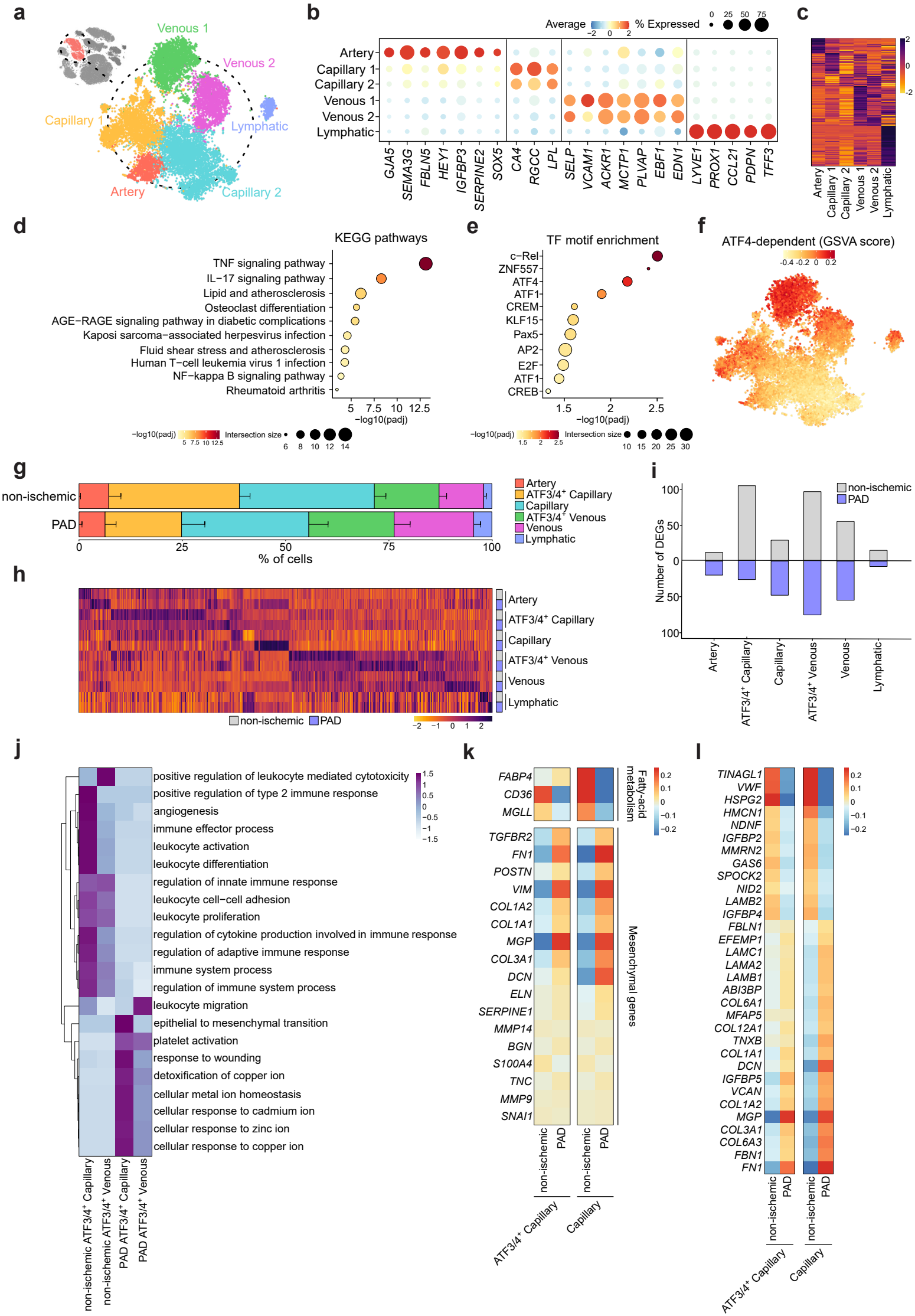
a
Venous 1
Venous 2
Capillary 1
Lymphatic
Artery
Capillary 2
b
Average
% Expressed
Artery
Capillary 1
Capillary 2
Venous 1
Venous 2
Lymphatic
GJA5
SEMA3G
FBLN5
HEY1
IGFBP3
SERPINE2
SOX5
CA4
RGCC
LPL
SELP
VCAM1
ACKR1
MCTP1
PLVAP
EBF1
EDN1
LYVE1
PROX1
CCL21
PDPN
TFF3
c
Artery
Capillary 1
Capillary 2
Venous 1
Venous 2
Lymphatic
d
KEGG pathways
TNF signaling pathway
IL−17 signaling pathway
Lipid and atherosclerosis
Osteoclast differentiation
AGE−RAGE signaling pathway in diabetic complications
Kaposi sarcoma−associated herpesvirus infection
Fluid shear stress and atherosclerosis
Human T−cell leukemia virus 1 infection
NF−kappa B signaling pathway
Rheumatoid arthritis
−log10(padj)
Intersection size
e
TF motif enrichment
c−Rel
ZNF557
ATF4
ATF1
CREM
KLF15
Pax5
AP2
E2F
ATF1
CREB
−log10(padj)
Intersection size
f
ATF4-dependent (GSVA score)
g
non-ischemic
PAD
% of cells
Artery
ATF3/4⁺ Capillary
Capillary
ATF3/4⁺ Venous
Venous
Lymphatic
h
Artery
ATF3/4⁺ Capillary
Capillary
ATF3/4⁺ Venous
Venous
Lymphatic
non-ischemic
PAD
i
non-ischemic
PAD
Number of DEGs
Artery
ATF3/4⁺ Capillary
Capillary
ATF3/4⁺ Venous
Venous
Lymphatic
j
positive regulation of leukocyte mediated cytotoxicity
positive regulation of type 2 immune response
angiogenesis
immune effector process
leukocyte activation
leukocyte differentiation
regulation of innate immune response
leukocyte cell−cell adhesion
leukocyte proliferation
regulation of cytokine production involved in immune response
regulation of adaptive immune response
immune system process
regulation of immune system process
leukocyte migration
epithelial to mesenchymal transition
platelet activation
response to wounding
detoxification of copper ion
cellular metal ion homeostasis
cellular response to cadmium ion
cellular response to zinc ion
cellular response to copper ion
non-ischemic ATF3/4⁺ Capillary
non-ischemic ATF3/4⁺ Venous
PAD ATF3/4⁺ Capillary
PAD ATF3/4⁺ Venous
k
FABP4
CD36
MGLL
Fatty-acid metabolism
TGFBR2
FN1
POSTN
VIM
COL1A2
COL1A1
MGP
COL3A1
DCN
ELN
SERPINE1
MMP14
BGN
S100A4
TNC
MMP9
SNAI1
Mesenchymal genes
non-ischemic
PAD
ATF3/4⁺ Capillary
Capillary
l
TINAGL1
VWF
HSPG2
HMCN1
NDNF
IGFBP2
MMRN2
GAS6
SPOCK2
NID2
LAMB2
IGFBP4
FBLN1
EFEMP1
LAMC1
LAMA2
LAMB1
ABI3BP
COL6A1
MFAP5
COL12A1
TNXB
COL1A1
DCN
IGFBP5
VCAN
COL1A2
MGP
COL3A1
COL6A3
FBN1
FN1
non-ischemic
PAD
ATF3/4⁺ Capillary
Capillary

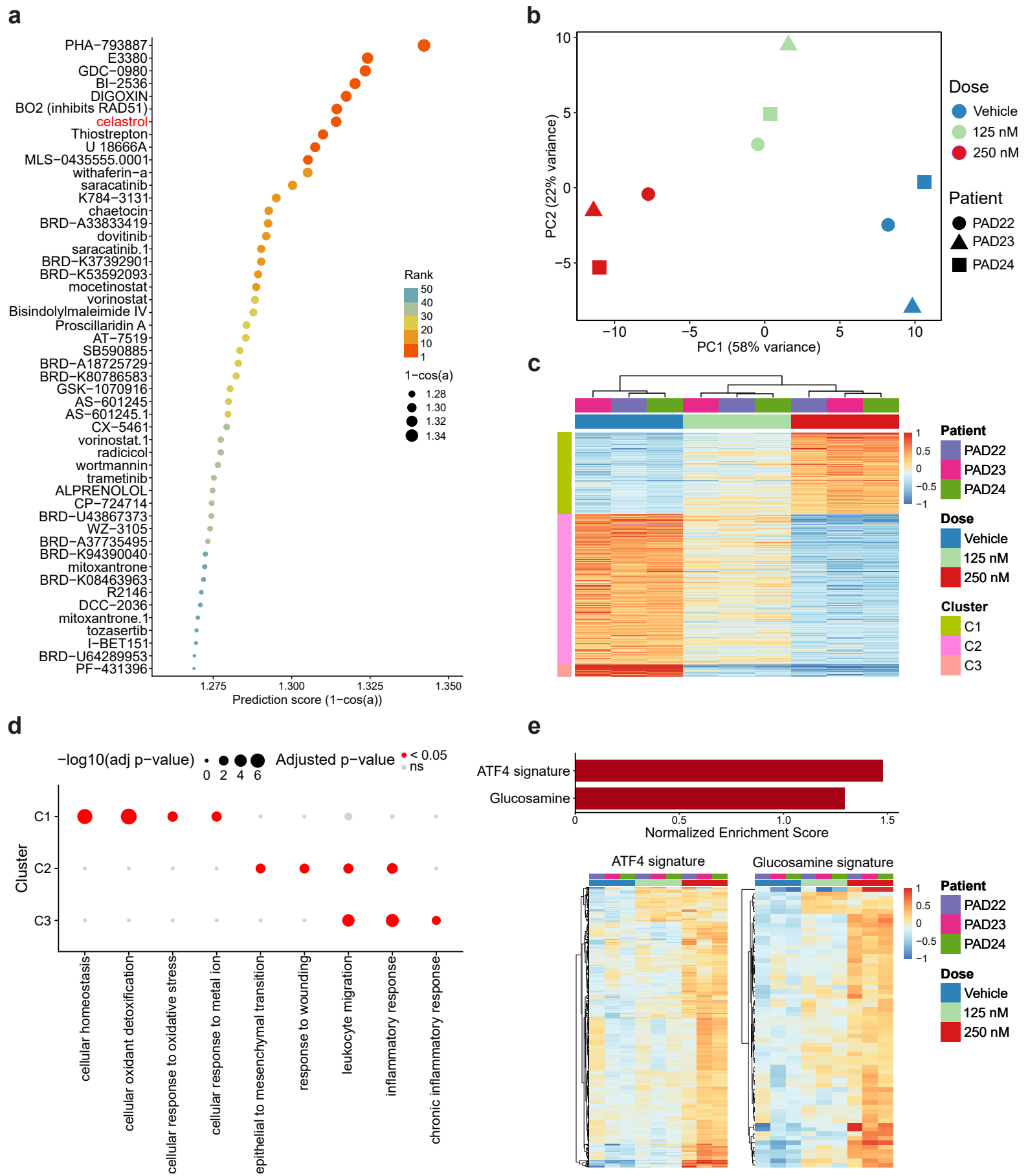
a
PHA−793887
E3380
GDC−0980
BI−2536
DIGOXIN
BO2 (inhibits RAD51)
celastrol
Thiostrepton
U 18666A
MLS−0435555.0001
withaferin−a
saracatinib
K784−3131
chaetocin
BRD−A33833419
dovitinib
saracatinib.1
BRD−K37392901
BRD−K53592093
mocetinostat
vorinostat
Bisindolylmaleimide IV
Proscillaridin A
AT−7519
SB590885
BRD−A18725729
BRD−K80786583
GSK−1070916
AS−601245
AS−601245.1
CX−5461
vorinostat.1
radicicol
wortmannin
trametinib
ALPRENOLOL
CP−724714
BRD−U43867373
WZ−3105
BRD−A37735495
BRD−K94390040
mitoxantrone
BRD−K08463963
R2146
DCC−2036
mitoxantrone.1
tozasertib
I−BET151
BRD−U64289953
PF−431396
1.275
1.300
1.325
1.350
Prediction score (1−cos(a))
Rank
50
40
30
20
10
1
1−cos(a)
1.28
1.30
1.32
1.34
b
PC2 (22% variance)
PC1 (58% variance)
10
5
0
−5
−10
Dose
Vehicle
125 nM
250 nM
Patient
PAD22
PAD23
PAD24
c
Patient
PAD22
PAD23
PAD24
Dose
Vehicle
125 nM
250 nM
Cluster
C1
C2
C3
1
0.5
0
−0.5
−1
d
−log10(adj p−value)
0 2 4 6
Adjusted p−value
< 0.05
ns
Cluster
C1
C2
C3
cellular homeostasis
cellular oxidant detoxification
cellular response to oxidative stress
cellular response to metal ion
epithelial to mesenchymal transition
response to wounding
leukocyte migration
inflammatory response
chronic inflammatory response
e
ATF4 signature
Glucosamine
0
0.5
1.0
1.5
Normalized Enrichment Score
ATF4 signature
Glucosamine signature
Patient
PAD22
PAD23
PAD24
Dose
Vehicle
125 nM
250 nM
1
0.5
0
−0.5
−1

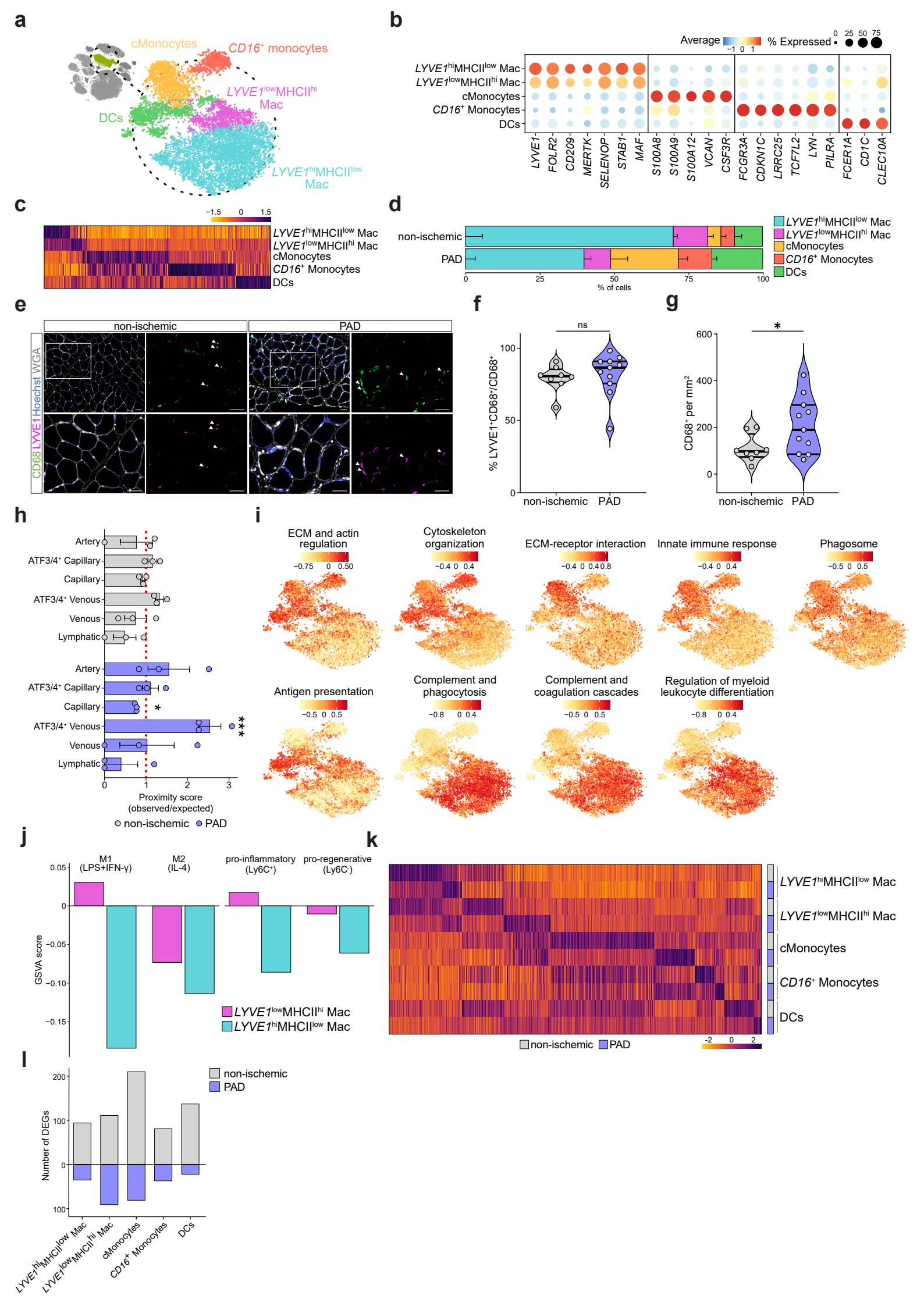
a
cMonocytes
CD16+ monocytes
LYVE1lowMHCIIhi Mac
DCs
LYVE1hiMHCIIlow Mac
b
Average
% Expressed
LYVE1hiMHCIIlow Mac
LYVE1lowMHCIIhi Mac
cMonocytes
CD16+ Monocytes
DCs
LYVE1 FOLR2 CD209 MERTK SELENOP STAB1 MAF
S100A8 S100A9 S100A12 VCAN CSF3R
FCGR3A CDKN1C LRRC25 TCF7L2 LYN PILRA
FCER1A CD1C CLEC10A
c
LYVE1hiMHCIIlow Mac
LYVE1lowMHCIIhi Mac
cMonocytes
CD16+ Monocytes
DCs
d
non-ischemic
PAD
% of cells
e
non-ischemic
PAD
CD68 LYVE1 Hoechst WGA
f
ns
% LYVE1+CD68-/CD68+
non-ischemic
PAD
g
*
CD68+ per mm2
non-ischemic
PAD
h
Artery
ATF3/4+ Capillary
Capillary
ATF3/4+ Venous
Venous
Lymphatic
Proximity score
(observed/expected)
non-ischemic
PAD
i
ECM and actin regulation
Cytoskeleton organization
ECM-receptor interaction
Innate immune response
Phagosome
Antigen presentation
Complement and phagocytosis
Complement and coagulation cascades
Regulation of myeloid leukocyte differentiation
j
M1 (LPS+IFN-γ)
M2 (IL-4)
pro-inflammatory (Ly6C+)
pro-regenerative (Ly6C-)
GSVA score
LYVE1lowMHCIIhi Mac
LYVE1hiMHCIIlow Mac
k
LYVE1hiMHCIIlow Mac
LYVE1lowMHCIIhi Mac
cMonocytes
CD16+ Monocytes
DCs
non-ischemic
PAD
l
non-ischemic
PAD
Number of DEGs
LYVE1hiMHCIIlow Mac
LYVE1lowMHCIIhi Mac
cMonocytes
CD16+ Monocytes
DCs

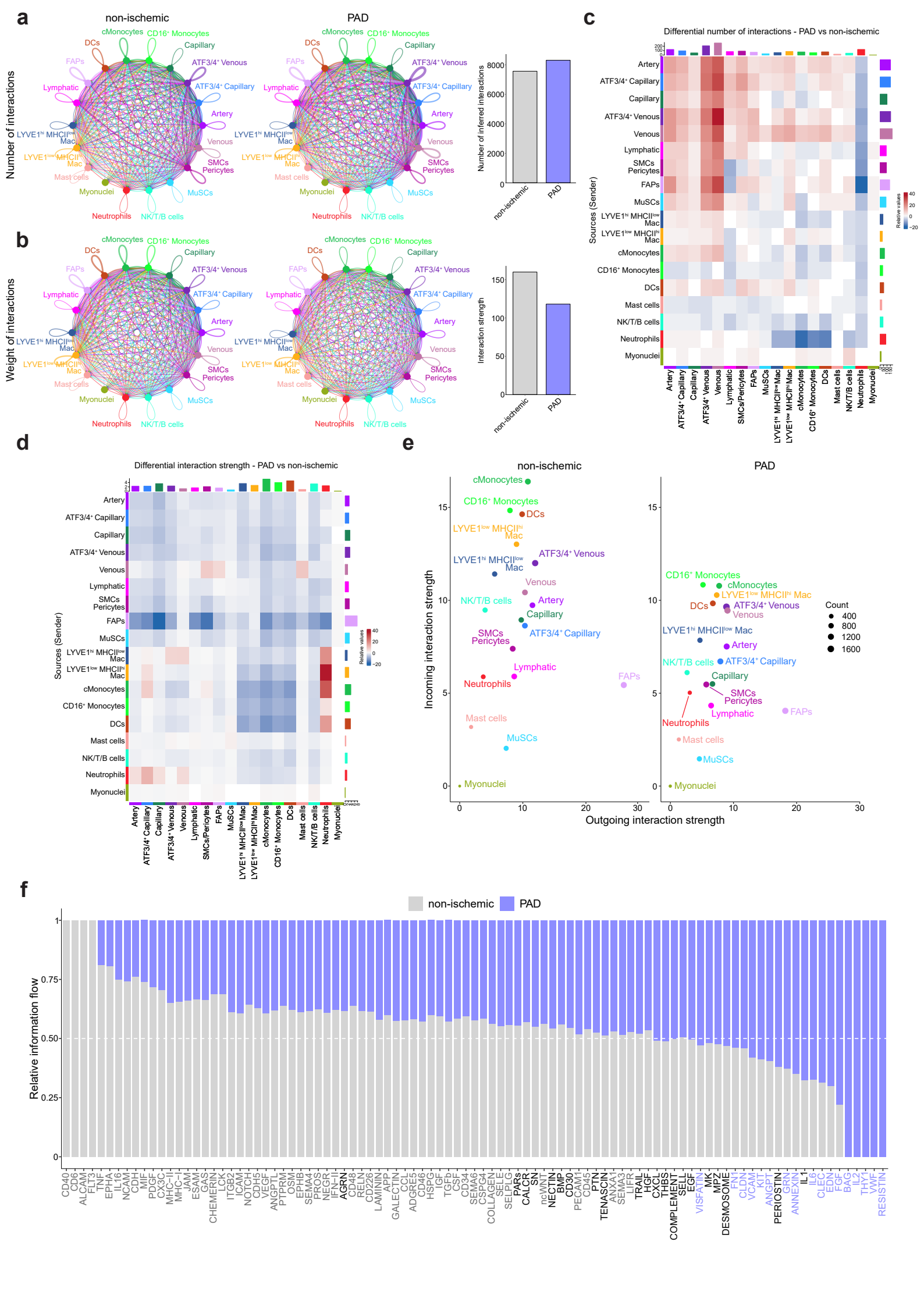
a
non-ischemic
PAD
Number of interactions
cMonocytes
CD16+ Monocytes
DCs
Capillary
FAPs
ATF3/4+ Venous
Lymphatic
ATF3/4+ Capillary
Artery
LYVE1hi MHCIIlow Mac
Venous
LYVE1low MHCIIhi Mac
SMCs Pericytes
Mast cells
Myonuclei
MuSCs
Neutrophils
NK/T/B cells
Number of inferred interactions
non-ischemic
PAD
b
Weight of interactions
Interaction strength
c
Differential number of interactions - PAD vs non-ischemic
Sources (Sender)
Relative values
d
Differential interaction strength - PAD vs non-ischemic
Sources (Sender)
Relative values
e
non-ischemic
PAD
Incoming interaction strength
Outgoing interaction strength
Count
f
non-ischemic
PAD
Relative information flow

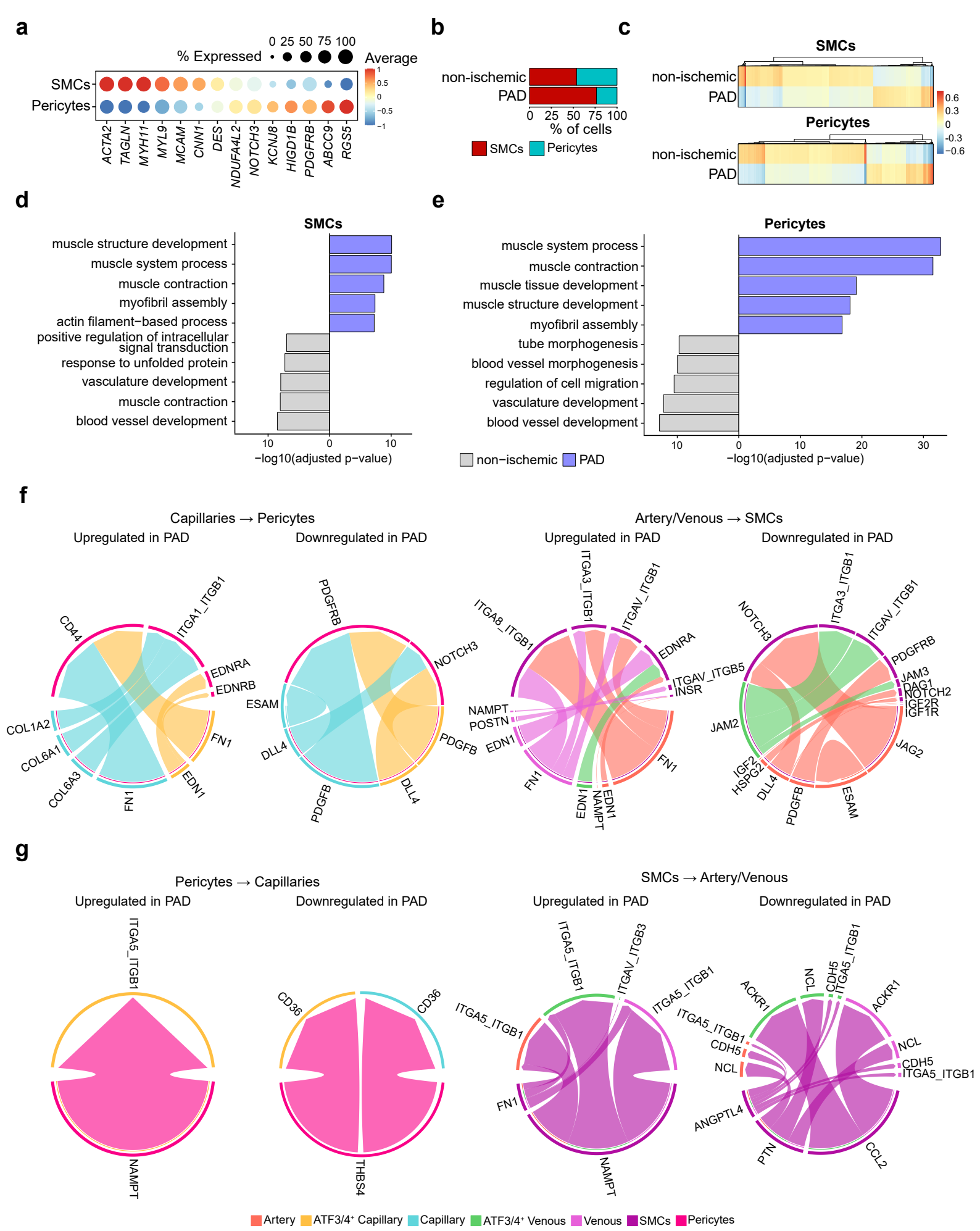
a
% Expressed
0 25 50 75 100
Average
SMCs
Pericytes
ACTA2
TAGLN
MYH11
MYL9
MCAM
CNN1
DES
NDUFA4L2
NOTCH3
KCNJ8
HIGD1B
PDGFRB
ABCC9
RGS5
b
non-ischemic
PAD
% of cells
SMCs
Pericytes
c
SMCs
Pericytes
d
SMCs
muscle structure development
muscle system process
muscle contraction
myofibril assembly
actin filament−based process
positive regulation of intracellular signal transduction
response to unfolded protein
vasculature development
muscle contraction
blood vessel development
−log10(adjusted p−value)
e
Pericytes
muscle system process
muscle contraction
muscle tissue development
muscle structure development
myofibril assembly
tube morphogenesis
blood vessel morphogenesis
regulation of cell migration
vasculature development
blood vessel development
non−ischemic
PAD
−log10(adjusted p−value)
f
Capillaries → Pericytes
Upregulated in PAD
Downregulated in PAD
Artery/Venous → SMCs
Upregulated in PAD
Downregulated in PAD
CD44
ITGA1_ITGB1
EDNRA
EDNRB
FN1
EDN1
COL6A3
COL6A1
COL1A2
PDGFRB
NOTCH3
PDGFB
DLL4
ESAM
ITGA8_ITGB1
ITGA3_ITGB1
ITGAV_ITGB1
EDNRA
ITGAV_ITGB5
INSR
FN1
EDN1
NAMPT
POSTN
NOTCH3
ITGA3_ITGB1
ITGAV_ITGB1
PDGFRB
JAM3
DAG1
NOTCH2
IGF2R
IGF1R
JAG2
ESAM
PDGFB
DLL4
HSPG2
IGF2
JAM2
g
Pericytes → Capillaries
Upregulated in PAD
Downregulated in PAD
SMCs → Artery/Venous
Upregulated in PAD
Downregulated in PAD
ITGA5_ITGB1
NAMPT
CD36
THBS4
ITGA5_ITGB1
ITGAV_ITGB3
FN1
NAMPT
ACKR1
NCL
CDH5
ITGA5_ITGB1
ANGPTL4
PTN
CCL2
Artery
ATF3/4⁺ Capillary
Capillary
ATF3/4⁺ Venous
Venous
SMCs
Pericytes

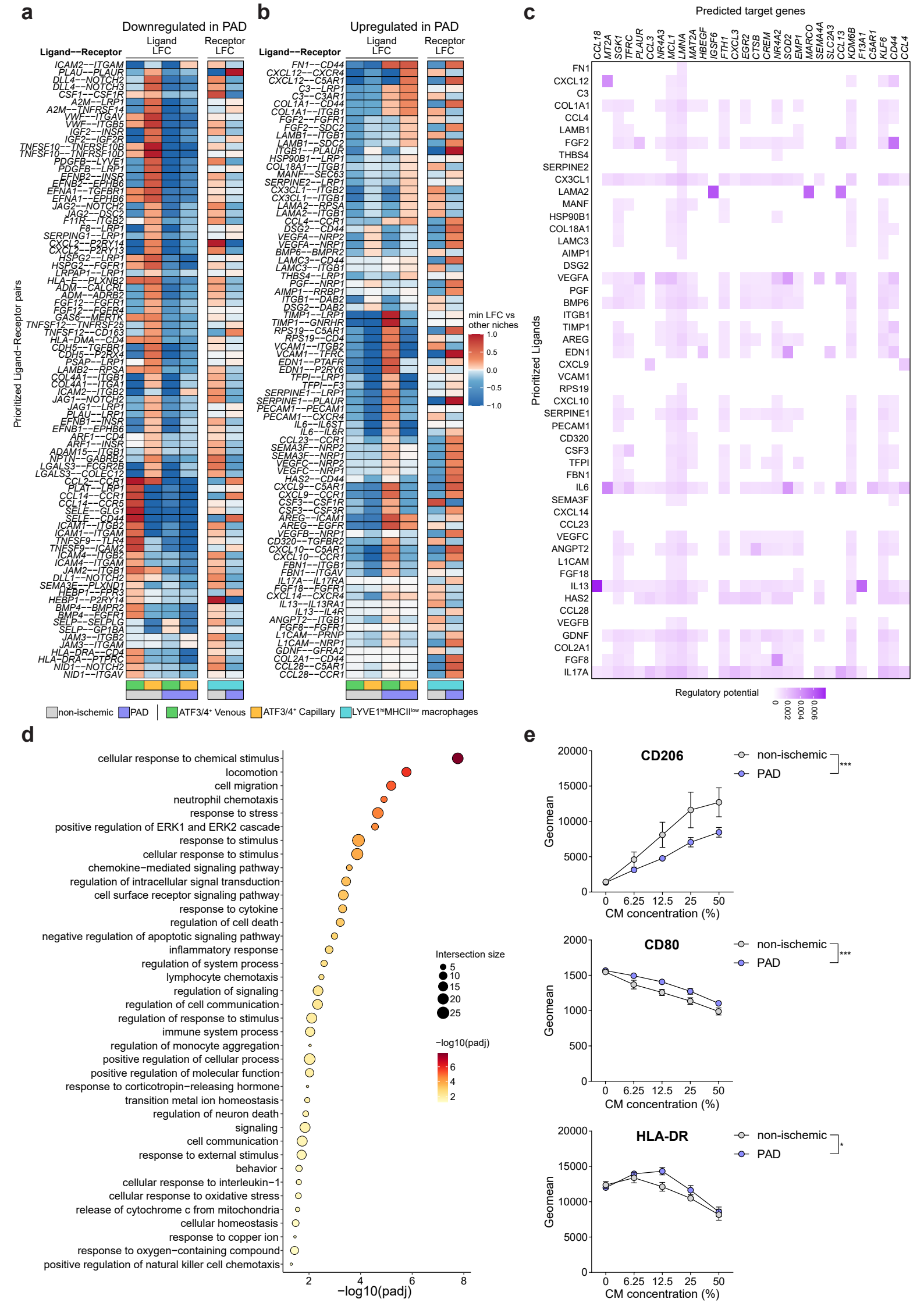
a
Downregulated in PAD
Ligand LFC
Receptor LFC
Ligand−Receptor
Prioritized Ligand−Receptor pairs
b
Upregulated in PAD
Ligand LFC
Receptor LFC
Ligand−Receptor
min LFC vs other niches
1.0
0.5
0.0
−0.5
−1.0
non-ischemic
PAD
ATF3/4⁺ Venous
ATF3/4⁺ Capillary
LYVE1ʰⁱMHCIIˡᵒʷ macrophages
c
Predicted target genes
Prioritized Ligands
Regulatory potential
0
0.002
0.004
0.006
d
cellular response to chemical stimulus
locomotion
cell migration
neutrophil chemotaxis
response to stress
positive regulation of ERK1 and ERK2 cascade
response to stimulus
cellular response to stimulus
chemokine−mediated signaling pathway
regulation of intracellular signal transduction
cell surface receptor signaling pathway
response to cytokine
regulation of cell death
negative regulation of apoptotic signaling pathway
inflammatory response
regulation of system process
lymphocyte chemotaxis
regulation of signaling
regulation of cell communication
regulation of response to stimulus
immune system process
regulation of monocyte aggregation
positive regulation of cellular process
positive regulation of molecular function
response to corticotropin−releasing hormone
transition metal ion homeostasis
regulation of neuron death
signaling
cell communication
response to external stimulus
behavior
cellular response to interleukin−1
cellular response to oxidative stress
release of cytochrome c from mitochondria
cellular homeostasis
response to copper ion
response to oxygen−containing compound
positive regulation of natural killer cell chemotaxis
−log10(padj)
Intersection size
5
10
15
20
25
−log10(padj)
6
4
2
e
CD206
CD80
HLA-DR
Geomean
CM concentration (%)
0
6.25
12.5
25
50
non-ischemic
PAD
***
*